PNAS

Main Manuscript for

Promoting C–F bond activation via proton donor for CF_4 decomposition

Yingkang Chen[a], Wenqiang Qu[b], Tao Luo[a], Hang Zhang[a], Junwei Fu[a], Hongmei Li[a], Changxu Liu[c], Dengsong Zhang[b], and Min Liu[a,*]

[a] Hunan Joint International Research Center for Carbon Dioxide Resource Utilization, School of Physics, and School of Metallurgy and Environment, Central South University, Changsha 410083, Hunan, P. R. China

[b] International Joint Laboratory of Catalytic Chemistry, Department of Chemistry, College of Sciences, Shanghai University, Shanghai 200444, P. R. China

[c] Centre for Metamaterial Research & Innovation, Department of Engineering, University of Exeter, Exeter EX4 4QF, United Kingdom

*Min Liu

Email: minliu@csu.edu.cn

Author Contributions: Y. C., D. Z., M. L. designed research; Y. C., H. Z. performed research; Y. C., T. L., H. Z., J. F., M. L. contributed new reagents/analytic tools; Y. C., W. Q., T. L., J. F., H. L., D. Z., M. L. analyzed data; and Y. C., W. Q., J. F., C. L., D. Z., M. L. wrote the paper.

Competing Interest Statement: The authors declare no competing interest.

Classification: Physical sciences; Chemistry.

Keywords: C–F bond activation | greenhouse effect | catalysis | proton donor | CF_4 hydrolysis

This PDF file includes:

Main Text
Figures 1 to 4

Abstract

Tetrafluoromethane (CF_4), the simplest perfluorocarbons (PFCs), is a permanently potent greenhouse gas due to its powerful infrared radiation adsorption capacity. The highly symmetric and robust C–F bond structure makes its activation a great challenge. Herein, we presented an innovated approach that efficiently activates C–F bond utilizing protonated sulfate ($–HSO_4$) modified Al_2O_3@ZrO_2 (S-Al_2O_3@ZrO_2) catalyst, resulting in highly efficient CF_4 decomposition. By combining *in situ* infrared spectroscopy tests and density function theory simulations, we demonstrate that the introduced $–HSO_4$ proton donor has a stronger interaction on the C–F bond than the hydroxyl (–OH) proton donor, which can effectively stretch the C–F bond for its activation. Consequently, the obtained S-Al_2O_3@ZrO_2 catalyst achieved a stable 100% CF_4 decomposition at a record low temperature of 580 °C with a turnover frequency (TOF) value of ~8.3 times higher than the Al_2O_3@ZrO_2 catalyst without $–HSO_4$ modification, outperforming the previously reported results. This work paves a new way for achieving efficient C–F bond activation to decompose CF_4 at a low temperature.

Significance Statement

Tetrafluoromethane (CF_4), also known as carbon tetrafluoride, is a permanent potent greenhouse gas. It finds extensive use in semiconductor manufacturing, and is the main by-product released during the smelting of electrolytic aluminum and rare earth metals. Due to the lack of effective treatment means, the concentration of CF_4 in the atmosphere has been increasing yearly. While thermal catalytic technology can decompose CF_4, but the high reaction temperature and low activity restrict its practical applications. Here, we developed a novel and effective strategy for CF_4 decomposition, achieving efficient decomposition at a record low reaction temperature. Our findings hold significant promise in the context of global warming, offering practical and impactful solutions to combat the detrimental effects of greenhouse gases.

Main Text

Introduction

Global warming has emerged as one of the most pressing concerns in the 21st century (1-3). Perfluorocarbons (PFCs) have alarmed widespread attention due to their potent greenhouse effects (4-7). Notably, the Carbon Border Adjustment Mechanism (CBAM) issued by European Union has listed PFCs among the greenhouse gases to be accounted for (8). Among them, tetrafluoromethane (CF_4), being the simplest and maximum concentrated PFCs in the atmosphere, possesses a remarkably high global warming potential (GWP) of 7,390 and extraordinarily long atmospheric lifetime of 50,000 years (9-14). Considering the doubling of its atmospheric concentration since the pre-industrial era (15), the development of a cost-effective CF_4 decomposition method becomes crucially important and highly desirable for achieving a sustainable future.

Among various CF_4 decomposition methods, the thermocatalytic hydrolysis process stands out due to its improved decomposition rate, no toxic by-products and large-scale applications potential (16-21). While the highly symmetrical single carbon structure and C–F bond with strong ionic character make CF_4 decomposition require a high temperature (22), the introduction of the catalyst can significantly promote the C–F bond activation and decrease the decomposition temperature. Takita et al. (16) first proposed that CF_4 could be hydrolyzed over Ce10%-$AlPO_4$ at 700 °C, well below its pyrolysis of 1200 °C (23). El-Bahy et al. (19) found that the introduction of Ga promoted C–F bond activation by increasing Lewis (L) acid sites on γ-Al_2O_3 surface, achieving a 84% CF_4 decomposition at 630 °C. Takashi et al. (24) reported that the Zn modified γ-Al_2O_3 catalyst with high density of strong L acid sites could completely hydrolyze CF_4 at 650 °C. Our previous study (21) revealed the relationship between the L acid strength of γ-Al_2O_3 surface site and its CF_4 decomposition ability. We found that the tri-coordination Al (Al_{III}) sites with the strong L acidity were the main active site for CF_4 decomposition.

Despite the aforementioned progress in reducing temperature, the CF_4 hydrolysis at beyond 600 °C still falls short of the desired efficiency for energy utilization. In addition to metal L acid sites (25, 26), Glusker et al. (27) discovered that the proton donor was also capable of interacting with C–F bond to activate it. For example, the hydroxyl (OH) groups could interact with C–F bond to promote fluorochemical decomposition (28-30). The interaction strength with C–F bond was affected by the type of the proton donor (27, 31-33). Thus, it could be predicted that the C–F bond of CF_4 could be further activated by modulating the proton donor on catalyst surface.

Herein, we achieve stable CF_4 decomposition with an efficiency of 100% operating at 580 °C, under a significantly reduced temperature. Through density function theory (DFT) simulations, we unveil that the introduced protonated sulfate ($–HSO_4$) strongly stretches the C–F bond of adsorbed CF_4 and facilitates its activation, which is experimentally verified by *in situ* infrared spectroscopy (*in situ* IR) tests. To capitalize on this insight, we design and fabricate a novel catalyst, composed of sulfated Al_2O_3 dispersed on ZrO_2 nanosheet (S-Al_2O_3@ZrO_2). A combination of X-ray photoelectron spectroscopy (XPS) and pyridine-infrared (py-IR) tests confirm the introduction of $–HSO_4$ proton donors on the S-Al_2O_3@ZrO_2 surface, facilitating a record low temperature for CF_4 decomposition. This work provides a new strategy for efficient C–F bond activation and CF_4 decomposition at low temperature, opening new avenues for sustainable catalysis with environmental benefits and promising energy efficiency.

Results and Discussion

Synthesis and Characterization.

S-Al_2O_3@ZrO_2 was prepared by modifying Al_2O_3@ZrO_2 with sulfuric acid, and calcined at 650 °C for 24 h to remove the excess sulfate species (*SI Appendix*, Fig. S1 and see *Materials and Methods* for details). X-ray diffraction (XRD) patterns of S-Al_2O_3@ZrO_2 showed only the characteristic peaks of tetragonal-ZrO_2 (PDF #79-1767), which was the same as that of unmodified Al_2O_3@ZrO_2 (Fig. 1*A*), revealing that sulfuric acid modification did not change the crystal structure of the catalysts. Brunauer-Emmett-Teller (BET) measurements (*SI Appendix*, Fig. S3 and Table S1) showed that the surface area slightly decreased from 61.3 m^2 g^{-1} (Al_2O_3@ZrO_2) to 49.8 m^2 g^{-1} (S-Al2O3@ZrO_2), further confirming no significant changes in its structure properties after sulfuric acid modification.

To detect the morphologies of the synthesized catalysts, transmission electron microscopy (TEM) was performed. The pristine ZrO_2 had a nanoparticle morphology with a size of ~25 nm (*SI Appendix*, Fig. S4a). Al_2O_3@ZrO_2 showed an identical nanoparticle morphology (*SI Appendix*, Fig. S4c) as the pristine ZrO_2, and its high-resolution TEM (HRTEM) image revealed the presence of Al_2O_3 (*SI Appendix*, Fig. S5d), indicating that Al_2O_3 was uniformly dispersed on ZrO_2 surface. After sulfuric acid modification, the morphology of S-Al_2O_3@ZrO_2 had no obvious change (Fig. 1*B*) compared with that of Al_2O_3@ZrO_2. In contrast, S-Al_2O_3 showed a significant agglomeration after sulfuric acid modification (*SI Appendix*, Fig. S4d), indicating that ZrO_2 ensured the uniform dispersion of Al_2O_3 during sulfuric acid modification process. Energy dispersive spectroscopy (EDS) mapping images of S-Al_2O_3@ZrO_2 (Fig. 1*C*) further proved the uniform distributions of S and Al on ZrO_2 surface.

To investigate the surface chemical environments of the S, O, Al and Zr in S-Al_2O_3@ZrO_2, XPS was carried out. The O 1s spectra (*SI Appendix*, Fig. S7) validated the presence of sulfate species on S-Al_2O_3@ZrO_2 after sulfuric acid modification. The sulfate species were further analyzed by S 2p spectra. The peaks at 169.0 eV and 170.3 eV of S-Al_2O_3@ZrO_2 could be attributed to $–SO_4$ and $–HSO_4$ (Fig. 1*D*), respectively (34), indicating the partial sulfate protonation on the catalyst surface. Meanwhile, the binding sites of $–HSO_4$ on S-Al_2O_3@ZrO_2 surface were investigated by Al 2p and Zr 3d spectra (Fig. 1*E* and 1*F*). The Al–O peaks (35) of S-Al_2O_3@ZrO_2 was shifted to higher energy region compared to that of Al_2O_3@ZrO_2, which could be attributed to the electron attracting effect of sulfate group to the surface Al site. However, no observable change could be found in Zr 3d region after sulfuric acid modification (Fig. 1*F* and *SI Appendix*, Fig. S10) (36), revealing the sulfate group was not bonded with Zr site. The coordination environment of the Zr sites in S-Al_2O_3@ZrO_2 was precisely characterized by synchrotron X-ray absorption spectroscopy (XAS) (*SI Appendix*, Fig. S11a) to further determine the binding sites of $–HSO_4$. The fitting result of Zr k-edge extended X-ray absorption fine structure (EXAFS) spectrum only found three scattering paths of Zr–O, Zr–Zr and Zr–Al (*SI Appendix*, Fig. S11b and Table S3), demonstrating that the introduced $–HSO_4$ proton donor was mainly bonded with Al site.

Properties of $–HSO_4$ Proton Donor.

To determine the properties of $–HSO_4$ proton donor, the surface acidity of $Al_2O_3@ZrO_2$ and S-$Al_2O_3@ZrO_2$ was investigated. First, the acid content and strength of the catalysts were tested by NH_3 temperature-programmed desorption (NH_3-TPD) (Fig. 2*A* and *SI Appendix*, Table S4). $Al_2O_3@ZrO_2$ showed three NH_3 desorption peaks, in which two desorption peaks below 200 °C were attributed to weak acid site, and one desorption peak between 200 °C and 300 °C was assigned to medium acid site (37). The desorption peak intensity and desorption temperature of S-$Al_2O_3@ZrO_2$ were obviously increased compared with those of $Al_2O_3@ZrO_2$, indicating a significant increase in acid content and strength via sulfuric acid modification. In particular, not only the medium acid peak of S-$Al_2O_3@ZrO_2$ was shifted to 300 °C and 400 °C, but also the medium acid amount increased from 3.63 $\mu mol\ g^{-1}$ ($Al_2O_3@ZrO_2$) to 12.11 $\mu mol\ g^{-1}$ (S-$Al_2O_3@ZrO_2$), demonstrating the S-$Al_2O_3@ZrO_2$ surface possessed more and stronger acid sites compared to that on $Al_2O_3@ZrO_2$. The increased strong acid sites were further analyzed by py-IR tests at different desorption temperature (Fig. 2*B*-2*D*). The observed bands at 1444 cm^{-1} and 1544 cm^{-1} can be assigned to pyridine adsorbed at L acid sites and Brønsted (B) acid sites, respectively (38). The results showed that $Al_2O_3@ZrO_2$ contained only L acid sites, and the B acid sites were introduced after sulfuric acid modification, which could be attributed to $–HSO_4$ (39, 40). The strong L acid sites were detected on both $Al_2O_3@ZrO_2$ and S-$Al_2O_3@ZrO_2$ catalysts upon desorption at 100 °C (Fig. 2*C*). Combined with the γ-Al_2O_3 (110) facet exposure observed in HRTEM results (*SI Appendix*, Fig. S5d and S5e), it could be determined that the detected strong L acid sites were Al_{III} sites with strong CF_4 adsorption. With the desorption temperature rising to 200 °C (Fig. 2*D*), the band corresponding to L acid sites on $Al_2O_3@ZrO_2$ and S-$Al_2O_3@ZrO_2$ disappeared, and the band corresponding to B acid sites was observed only on S-$Al_2O_3@ZrO_2$, indicating the B acid sites in S-$Al_2O_3@ZrO_2$ had strong acidity. This result confirmed that the introduced $–HSO_4$ proton donor has a strong proton donating ability.

Influence of $–HSO_4$ Proton Donor on C–F Bond Activation.

To investigate the influence of $–HSO_4$ proton donor on C–F bond activation, the *in situ* IR spectra of S-$Al_2O_3@ZrO_2$ at 580 °C were tested under CF_4 atmosphere (Fig. 3*A*). The bands of CF_4 decomposition product HF (3741, 3785, 3832, 3877 and 3920 cm^{-1}) (41) were detected, indicating that the C–F bond could be directly activation on S-$Al_2O_3@ZrO_2$ surface. Meanwhile, the depletion of $–HSO_4$ (1026 cm^{-1}) (42) and the production of $–SO_4$ (998, 1072 and 1142 cm^{-1}) (36, 43) revealed that the C–F bond was activated by $–HSO_4$ and generated $–SO_4$ and HF.

To determine the C–F bond activation with $–HSO_4$ during CF_4 hydrolysis, the *in situ* IR spectra of S-$Al_2O_3@ZrO_2$ at 580 °C were tested under CF_4 and H_2O atmosphere and only H_2O atmosphere, respectively (Fig. 3*B*). When feed with CF_4 and H_2O simultaneously, the production of HF and $–SO_4$ as well as the depletion of $–HSO_4$ were observed, which was similar to the case with CF_4 only, indicating $–HSO_4$ directly involved in C–F bond activation with or without H_2O. After switching to H_2O only (Fig. 3*B*), it could be found that the $–SO_4$ bands gradually disappeared, while the regeneration of $–HSO_4$ was observed. The results demonstrated that the stable C–F bond activation could be achieved with $–HSO_4$ during CF_4 hydrolysis, and $–HSO_4$ could be regenerated by H_2O dissociation over S-$Al_2O_3@ZrO_2$.

The effect of proton donor on C–F bond activation was further investigated by DFT calculations. On the basis of γ-Al_2O_3 (110) facet containing Al_{III} site (*SI Appendix*, Fig. S17), the CF_4 adsorption energy at Al_{III} site (E_{ads}) and C–F bond length were calculated on three different models of γ-Al_2O_3, γ-Al_2O_3 with –OH (γ-Al_2O_3–OH) and γ-Al_2O_3 with $–HSO_4$ (γ-Al_2O_3–HSO_4), respectively (Fig. 3*C*). The calculation results showed that the E_{ads} of γ-Al_2O_3–HSO_4 was −0.64 eV, which was much stronger than those of γ-Al_2O_3–OH (−0.51 eV) and γ-Al_2O_3 (−0.44 eV) (Fig. 3*D*), indicating that the CF_4 adsorption was significantly enhanced by introducing $–HSO_4$. The CF_4-temperature programed desorption (CF_4-TPD) results of $Al_2O_3@ZrO_2$ and S-$Al_2O_3@ZrO_2$

(Fig. 3*E*) also proved this result, as the CF_4 desorption temperature of S-Al_2O_3@ZrO_2 was significantly increased after sulfuric acid modification. On the other hand, the C–F bond length on γ-Al_2O_3–HSO_4 increased from 1.36 Å to 1.45 Å, which was larger than that on γ-Al_2O_3 (1.42 Å) and γ-Al_2O_3–OH (1.43 Å) (Fig. 3*D*). The enhanced adsorption and molecular deformation of CF_4 proved that –HSO_4 can promote the C–F bond activation. Based on these results, a synergistic mechanism for C–F bond activation was proposed (Fig. 3*F*). The Al_{III} site stably securely CF_4 molecule, while the adjacent –HSO_4 proton donor generates the H···C–F interaction with the adsorbed CF_4. The synergistic stretching effect of Al_{III}-HSO_4 pair sites on CF_4 promotes the C–F bond activation.

CF_4 Hydrolysis Performance.

In order to determine the promotion of –HSO_4 for C–F bond activation, the CF_4 hydrolysis performances were tested under 440 to 660 °C (Fig. 4*A* and *SI Appendix*, Fig. S20). The S-Al_2O_3@ZrO_2 catalyst with abundant –HSO_4 showed excellent CF_4 hydrolysis activity and could stably achieve 100% CF_4 decomposition at the temperature (T_{100}) of 580 °C (Fig. 4*B*), which was much lower than that of Al_2O_3@ZrO_2 (660 °C) and other previously reported catalysts (*SI Appendix*, Table S5), proving the great promotion of C–F bond activation by the introduction of –HSO_4 proton donor. Similarly, the CF_4 hydrolysis test results on Al_2O_3 (640 °C) and S-Al_2O_3 (620 °C) also demonstrated this promoted effect. The S-Al_2O_3@ZrO_2 catalyst after stability test was then characterized (*SI Appendix*, Fig. S21-S24, and Table S7 and S8). It could be found that the surface –HSO_4 proton donor content remained almost unchanged. The key effect of –HSO_4 in promoting C–F bond activation was further demonstrated.

Combined with the above DFT simulations and previous report (21), Al_{III} site is the main active site for CF_4 decomposition. The turnover frequency (TOF) values at 500 °C were calculated according to the content of surface Al_{III} site determined by the results of surface acidity test (*SI Appendix*, Table S4). The results demonstrated the significantly enhanced of the catalyst intrinsic activity after introducing –HSO_4 proton donor, and the S-Al_2O_3@ZrO_2 catalyst presented the highest TOF of 3.91×10^{-3} s^{-1}, which was ~8.3 times as that of Al_2O_3@ZrO_2 (0.47×10^{-3} s^{-1}). Further, the activation energies (E_a) of CF_4 over different catalysts (Fig. 4*C*) was evaluated by the CF_4 hydrolysis reaction rates (Fig. 4*D*). The results showed that the E_a of both S-Al_2O_3 and S-Al_2O_3@ZrO_2 were significantly reduced compared with those before sulfuric acid modification, demonstrating the activation of CF_4 molecules by –HSO_4. Especially, the S-Al_2O_3@ZrO_2 had the lowest E_a of 86.5 kJ mol^{-1}, corresponding to its efficient CF_4 decomposition.

Conclusion

In summary, a strategy to active the C–F bond for effective CF_4 decomposition has been proposed by enhancing the interaction between –HSO_4 proton donor and C–F bond. The S-Al_2O_3@ZrO_2 catalyst with abundant –HSO_4 exhibited an excellent CF_4 hydrolysis activity, in which CF_4 was completely decomposed at a record low temperature of 580 °C with a TOF value ~8.3 times that of the Al_2O_3@ZrO_2 catalyst with –HSO_4. It was demonstrated that the enhanced interaction between the introduced –HSO_4 proton donor and the C–F bond was decisive to enhance CF_4 hydrolysis activity, verified by *in situ* IR test and DFT simulation. –HSO_4 had a stronger interaction with C–F bond than that of –OH could effectively activate the C–F bond, thus promoting CF_4 decomposition. This proposed strategy paves a way for the development of efficient C–F bond activation and CF_4 decomposition catalyst. As global warming continues to be a pressing concern, our findings open new avenues for practical and impactful solutions to combat the detrimental effects of greenhouse gases.

Materials and Methods

Materials.

All chemicals were obtained commercially and used as received. Zirconium oxychloride octahydrate ($ZrOCl_2 \cdot 8H_2O$, 99%) and aluminum nitrate nonahydrate ($Al(NO_3)_3 \cdot 9H_2O$, 99%) were purchased from Aladdin. Aqueous ammonia ($NH_3 \cdot H_2O$) and sulfuric acid (H_2SO_4) were purchased from Sinopharm.

Preparation of Al_2O_3@ZrO_2.

Al_2O_3@ZrO_2 was synthesized using the hydrothermal method. Firstly, 30 mM (9.7 g) $ZrOCl_2 \cdot 8H_2O$ and 3.6 mM (1.4 g) $Al(NO_3)_3 \cdot 9H_2O$ were dissolved in 100 mL of deionized water by stirring at room temperature, and $NH_3 \cdot H_2O$ was added till pH~10. Then, the above solution was transferred into a 150 mL Teflon-lined stainless-steel autoclave and kept at 150 °C for 24 h. After cooling to room temperature, the precipitate was washed with deionized water and dried under 60 °C overnight, and calcined in air at 600 °C (a heating rate of 3 °C min^{-1}) for 5 h. The pristine Al_2O_3 and ZrO_2 samples were obtained by the same method with only adding aluminum source and zirconium source, respectively.

Preparation of S-Al_2O_3@ZrO_2.

2.0 g Al_2O_3@ZrO_2 and 2.0 g Al_2O_3 samples were added to 10 mL of 1 M H_2SO_4 and dried overnight at 60 °C, and then calcined in air at 650 °C (a heating rate of 3 °C min^{-1}) for 24 h to obtain S-Al_2O_3@ZrO_2 and S-Al_2O_3, respectively.

Catalyst Characterization.

XRD patterns were obtained by using a STADIP automated transmission diffractometer, operated at 36 kV and 20 mA by using CuKa1 radiation. The XRD patterns were scanned in the 2 Theta range of 15-90°.

The TEM and EDS images were obtained by JEOL 3010 operated at 200 kV. The finely ground sample was dispersed in ethanol and then dropped onto a copper grid for TEM and EDX testing.

XPS was recorded on a Kratos Axis Ultra DLD X-ray photoelectron spectrometry, using a standard Al Ka X-ray source and an analyzer pass energy of 40 eV. All binding energies were referenced to the adventitious C 1s line at 284.6 eV.

The BET surface area and pore size distribution of the catalysts were determined by N_2 adsorption-desorption analysis using AUTOSORB IQ. Prior to measurements, the samples were degassed at 300 °C for 6 h, at a heating rate of 10 °C min^{-1}.

NH_3-TPD and CF_4-TPD were performed by using a PCA-1200 on a chemisorption analyzer equipped with a thermal conductivity detector (TCD). The chemisorption analyzer was carried out on the PCA-1200 from Beijing Builder electronic technology Co., Ltd. For each experiment, the weighed sample (100 mg) was pretreated at 600 °C (10 °C min^{-1}) for 2 h under Ar (30 mL min^{-1}) and cooled to room temperature. Then the NH_3 gas (30 mL min^{-1}) or 20% CF_4/Ar gas (30 mL min^{-1}) was introduced instead of Ar at this temperature for 1 h to ensure the saturation adsorption. The sample was then purged with Ar for 1 h (30 mL min^{-1}) until the signal returned to the baseline as monitored by a TCD. The desorption curve of NH_3 or CF_4 was acquired by heating the sample from room temperature to 800 °C (10 °C min^{-1}) under Ar with the flow rate of 30 mL min^{-1}.

Py-IR spectra of samples were analyzed by a Thermo IS-50 Fourier Transform infrared (FTIR) spectrometer. The sample was heated at 500 °C for 5 h, and cooled to room temperature. Then, vacuumized to 10^{-3} Torr, samples were exposed to pyridine vapour (3000 Pa) at 100 °C for 1 h, followed by reevacuation for 1 h, and lower the temperature to take out our samples. After this step, the sample was analyzed by FTIR.

In situ IR spectra of sample was also analyzed by a Thermo IS-50 FTIR spectrometer. Self-supported wafer was prepared from catalyst powder (ca. 10 mg). The wafer was loaded into an in-situ IR thermal catalytic cell with CaF_2 windows and pretreated under Ar flow at 600 °C for 2 h. Then regulated to the target temperature to obtain a background spectrum which should be deducted from the sample spectra. As for the transient reactions between (1) CF_4 and water vapor and (2) water vapor, after the background spectra at appointed temperatures under Ar flow was obtained, the catalysts were exposed to (1) 1 mL min^{-1} 20% CF_4/Ar + water vapor (50 mL Ar passing through water bottle) or (2) water vapor (50 mL Ar passing through water bottle) at 580 °C and meanwhile the reaction process was recorded as a function of time. For the adsorption of

CF_4 studies, after the same pretreatment, the catalysts were exposed to a flow of 20% CF_4/Ar at 100 °C for 2 h. The desorption process then went on under a flow of Ar, and the temperature was gradually raised to 700 °C (a step of 50 °C) and recorded as a function of temperature.

Catalytic Activity Evaluation and Analytical Methods.

CF_4 hydrolysis was measured by using a continuous flow reaction system with a quartz fixed-bed reactor (i.d. 20 mm) under atmospheric pressure in a temperature range from 440 to 660 °C. A gas flow of 33.3 mL min^{-1} (0.25% CF_4 in Ar) controlled by a mass flow controller, together with 0.2 mL h^{-1} of water pumped by an injection pump, were passed over 2.0 g of catalyst. According to the following equations, the CF_4 decomposition is calculated:

$$\mathrm{CF_4\ decomposition\ (\%)} = \frac{[\mathrm{CF_4}]_{\mathrm{in}} - [\mathrm{CF_4}]_{\mathrm{out}}}{[\mathrm{CF_4}]_{\mathrm{in}}} \times 100\%$$

where $[CF_4]_{in}$ and $[CF_4]_{out}$ indicate the input and output relative gas concentrations, respectively.

Theoretical Calculation Studies.

All our investigations in this study were based on density functional theory, as implemented in the Vienna ab initio simulation package (VASP) (44, 45). The exchange-correlation potential is treated with the Perdew-Burke- Ernzerhof (PBE) formula by using the projected augmented wave (PAW) method within the generalized gradient approximation (GGA) (46). The cut-off energy for all calculations was set to be 450 eV. All the positions of atoms are fully relaxed until the Hellmann-Feynman forces on each atom are less than 0.01 eV $Å^{-1}$. Meanwhile, a k-points Γ-centered mesh is generated for Brillouin zone samples. The DFT-D_3 method proposed by Grimme was adopted to describe the van der Waals interactions, which has been shown to accurately describe chemisorption and physisorption properties on layered material. In addition, A vacuum region of about 15 Å was used to decouple the periodic replicas.

Data, Materials, and Software Availability.

All study data are included in the article and/or *SI Appendix*.

Acknowledgments

We thank the National Natural Science Foundation of China (Grant Nos. 22002189, 22376222, 52202125 and 22125604), Science and Technology Innovation Program of Hunan Province (Grant No. 2023RC1012), Central South University Research Programme of Advanced Interdisciplinary Studies (Grant No. 2023QYJC012), Central South University Innovation-Driven Research Programme (Grant No. 2023CXQD042). We would like to acknowledge the help from Beam Lines BL01C1 in the National Synchrotron Radiation Research Center (NSRRC, Hsinchu, Taiwan) for various synchrotron-based measurements. We are grateful for technical support from the High Performance Computing Center of Central South University.

References

1. P. P. Bera, J. S. Francisco, T. J. Lee, Design strategies to minimize the radiative efficiency of global warming molecules. *Proc. Natl. Acad. Sci. U. S. A.* **107**, 9049-9054 (2010).
2. B. Bolin, H. S. Kheshgi, On strategies for reducing greenhouse gas emissions. *Proc. Natl. Acad. Sci. U. S. A.* **98**, 4850-4854 (2001).
3. A. Nauels, J. Gütschow, M. Mengel, M. Meinshausen, P. U. Clark, C.-F. Schleussner, Attributing long-term sea-level rise to Paris Agreement emission pledges. *Proc. Natl. Acad. Sci. U. S. A.* **116**, 23487-23492 (2019).
4. C. A. McMillan, G. A. Keoleian, Not all primary aluminum is created equal: Life cycle greenhouse gas emissions from 1990 to 2005. *Environ. Sci. Technol.* **43**, 1571-1577 (2009).
5. T. Saito, Y. Yokouchi, A. Stohl, S. Taguchi, H. Mukai, Large emissions of perfluorocarbons in

East Asia deduced from continuous atmospheric measurements. *Environ. Sci. Technol.* **44**, 4089-4095 (2010).

6. B. Gschrey, W. Schwarz, C. Elsner, R. Engelhardt, High increase of global F-gas emissions until 2050. *GHG Measur. and Manag* **1**, 85-92 (2011).
7. S. Choi, S. H. Hong, H. S. Lee, T. Watanabe, A comparative study of air and nitrogen thermal plasmas for PFCs decomposition. *Chem. Eng. J.* **185**, 193-200 (2012).
8. Europäische Union, Regulation (EU) 2023/956 of the European Parliament and of the council of 10 May 2023 establishing a carbon border adjustment mechanism. *Official Journal of the European Union* **66**, (2023).
9. S. Yang, H. Zhang, Z. Zou, J. Li, X. Zhong, Reducing PFCs with local anode effect detection and independently controlled feeders in aluminum reduction cells. *JOM* **72**, 229-238 (2020).
10. B. A. Wofford, M. W. Jackson, C. Hartz, J. W. Bevan, Surface wave plasma abatement of CHF_3 and CF_4 containing semiconductor process emissions. *Environ. Sci. Technol.* **33**, 1892-1897 (1999).
11. J. Harnisch, R. Borchers, P. Fabian, K. Kourtidis, Aluminium production as a source of atmospheric carbonyl sulfide (COS). *Environ. Sci. Pollut. Res.* **2**, 161-162 (1995).
12. J. H. Hildebrand, R. H. Lamoreaux, Diffusivity of gases in liquids. *Proc. Natl. Acad. Sci. U. S. A.* **71**, 3321-3324 (1974).
13. R. J. Cicerone, Atmospheric carbon tetrafluoride: A nearly inert gas. *Science* **206**, 59-61 (1979).
14. D. R. Worton, W. T. Sturges, L. K. Gohar, K. P. Shine, P. Martinerie, D. E. Oram, S. P. Humphrey, P. Begley, L. Gunn, J.-M. Barnola, Atmospheric trends and radiative forcings of CF_4 and C_2F_6 inferred from firn air. *Environ. Sci. Technol.* **41**, 2184-2189 (2007).
15. L. Hockstad, L. Hanel, Inventory of US greenhouse gas emissions and sinks. *Environmental System Science Data Infrastructure for a Virtual Ecosystem (ESS-DIVE) (United States)* (2018).
16. Y. Takita, M. Ninomiya, H. Miyake, H. Wakamatsu, Y. Oshinaga, T. Ishihara, Catalytic decomposition of perfluorocarbons part II. Decomposition of CF_4 over $AlPO_4$-rare earth phosphate catalysts. *Phys. Chem. Chem. Phys.* **1**, 4501-4504 (1999).
17. X. Xu, J. Y. Jeon, M. H. Choi, H. Y. Kim, W. C. Choi, Y. Park, The modification and stability of γ-Al_2O_3 based catalysts for hydrolytic decomposition of CF_4. *J. Mol. Catal. A-Chem.* **266**, 131-138 (2007).
18. J. Song, S. Chung, M. Kim, M. Seo, Y. Lee, K. Lee, J. Kim, The catalytic decomposition of CF_4 over Ce/Al_2O_3 modified by a cerium sulfate precursor. *J. Mol. Catal. A-Chem.* **370**, 50-55 (2013).
19. Z. M. El-Bahy, R. Ohnishi, M. Ichikawa, Hydrolytic decomposition of CF_4 over alumina-based binary metal oxide catalysts: high catalytic activity of gallia-alumina catalyst. *Catal. Today* **90**, 283-290 (2004).
20. Y. J. Jong, X. Xiu-Feng, H. C. Mi, Y. K. Hee, P. Yong-Ki, Hydrolytic decomposition of PFCs over $AlPO_4$-Al_2O_3 catalyst. *Chem. Commun.* 1244-1245 (2003).
21. H. Zhang, T. Luo, Y. Long, Y. Chen, J. Fu, H. Liu, J. Hu, Z. Lin, L. Cai, M. Liu, Identification of the active site during CF_4 hydrolytic decomposition over γ-Al_2O_3. *Environ. Sci.-Nano* **9**, 954-963 (2022).
22. A. Anus, M. Sheraz, S. Jeong, E. Kim, S. Kim, Catalytic thermal decomposition of tetrafluoromethane (CF_4): A review. *J. Anal. Appl. Pyrolysis* **156**, 105126 (2021).
23. H. Erguang, H. Zheng, W. Shukun, X. Liyong, B. Mengna, Thermal decomposition and interaction mechanism of HFC-227ea/n-hexane as a zeotropic working fluid for organic Rankine cycle. *Energy* **246**, 123435 (2022).
24. T. Sasaki, S. Kanno, Role of acid sites on γ-Al_2O_3 based catalyst for CF_4 hydrolysis. *Kag. Kog. Ronbunshu* **37**, 175-180 (2011).
25. W. Jia, Q. Wu, X. Lang, C. Hu, G. Zhao, J. Li, Z. Zhu, Influence of Lewis acidity on catalytic activity of the porous alumina for dehydrofluorination of 1,1,1,2-tetrafluoroethane to

trifluoroethylene. *Catal. Lett.* **145**, 654-661 (2015).

26. T. Stahl, H.-F. Klare, M. Oestreich, Main-group Lewis acids for C–F bond activation. *ACS Catal.* **3**, 1578-1587 (2013).
27. M. Rust, W. C. Stallings, R. K. Preston, Intermolecular interactions of the C–F bond: The crystallographic environment of fluorinated carboxylic acids and related structures. *J. Am. Chem. Soc.* **105**, 3206-3214 (1983).
28. R. S. P. Von, A. J. Kos, The importance of negative (anionic) hyperconjugation. *Tetrahedron* **39**, 1141-1150 (1983).
29. J. AK. Howard, V. J. Hoy, D. O'Hagan, G. T. Smith, How good is fluorine as a hydrogen bond acceptor? *Tetrahedron* **52**, 12613-12622 (1996).
30. R. A. Cormanich, R. Rittner, M. P. Freitas, M. Bühl, The seeming lack of CF···HO intramolecular hydrogen bonds in linear aliphatic fluoroalcohols in solution. *Phys. Chem. Chem. Phys.* **16**, 19212-19217 (2014).
31. P. A. Champagne, J. Desroches, J. F. Paquin, Organic fluorine as a hydrogen-bond acceptor: recent examples and applications. *Synthesis* **47**, 306-322 (2015).
32. P. A. Champagne, Y. Benhassine, J. Desroches, J. F. Paquin, Friedel-crafts reaction of benzyl fluorides: Selective activation of C–F bonds as enabled by hydrogen bonding. *Angew. Chem.-Int. Edit.* **53**, 13835-13839 (2014).
33. B. Nepal, S. Scheiner, Anionic CH···X− hydrogen bonds: Origin of their strength, geometry, and other properties. *Chem. Eur. J.* **21**, 1474-1481 (2015).
34. V. Pârvulescu, S. Coman, P. Grange, V. I. Pârvulescu, Preparation and characterization of sulfated zirconia catalysts obtained via various procedures. *Appl. Catal. A-Gen.* **176**, 27-43 (1999).
35. A. Makarowicz, C. L. Bailey, N. Weiher, E. Kemnitz, S. L. M. Schroeder, S. Mukhopadhyay, A. Wander, B. G. Searle, N. M. Harrison, Electronic structure of lewis acid sites on high surface area aluminium fluorides: A combined XPS and ab initio investigation. *Phys. Chem. Chem. Phys.* **11**, 5664-5673 (2009).
36. H. Wang, Y. Li, F. Yu, Q. Wang, B. Xing, D. Li, R. Li, A stable mesoporous super-acid nanocatalyst for eco-friendly synthesis of biodiesel. *Chem. Eng. J.* **364**, 111-122 (2019).
37. Y. Chen, H. Zhang, H. Li, J. Hu, Y. Long, M. Liu, Alumina catalyst with high density of medium acid sites for N-arylpyrrolidines synthesis. *Appl. Catal. A-Gen.* **640**, 118668 (2022).
38. H. Zhang, W. Yang, I. I. Roslan, S. Jaenicke, G. Chuah, A combo Zr-HY and Al-HY zeolite catalysts for the one-pot cascade transformation of biomass-derived furfural to γ-valerolactone. *J. Catal.* **375**, 56-67 (2019).
39. J. M. Dominguez, J. L. Hernandez, G. Sandoval, Surface and catalytic properties of Al_2O_3–ZrO_2 solid solutions prepared by sol–gel methods. *Appl. Catal. A-Gen.* **197**, 119-130 (2000).
40. A. I. Ahmed, S. A. El-Hakam, A. S. Khder, W. S. A. El-Yazeed, Nanostructure sulfated tin oxide as an efficient catalyst for the preparation of 7-hydroxy-4-methyl coumarin by Pechmann condensation reaction. *J. Mol. Catal. A-Chem.* **366**, 99-108 (2013).
41. M. Mosiadz, K. L. Juda, S. C. Hopkins, J. Soloducho, B. A. Glowacki, An in-depth *in situ* IR study of the thermal decomposition of barium trifluoroacetate hydrate. *Thermochim. Acta* **513**, 33-37 (2011).
42. L. Xiao-Fei, W. Kui, H. Chao, L. Jin-Hua, A. Xing-Tao, P. Jie, W. Qi, W. Guo-Ming, Y. Guo-Yu, $Sb_4O_3(TeO_3)_2(HSO_4)(OH)$: An antimony tellurite sulfate exhibiting large optical anisotropy activated by lone pair stereoactivity. *Inorg. Chem.* **62**, 7123-7129 (2023).
43. N. Lazaroff, W. Sigal, A. Wasserman, Iron oxidation and precipitation of ferric hydroxysulfates by resting thiobacillus ferrooxidans cells. *Appl. Environ. Microbiol.* **43**, 924-938 (1982).
44. G. Kresse, J. Hafner, Ab initio molecular dynamics for liquid metals. *Phys. Rev. B* **47**, 558 (1993).
45. G. Kresse, J. Furthmüller, Efficient iterative schemes for ab initio total-energy calculations using a plane-wave basis set. *Phys. Rev. B* **54**, 11169 (1996).
46. J. P. Perdew, K. Burke, M. Ernzerhof, Generalized gradient approximation made simple. *Phys. Rev. Lett.* **77**, 3865 (1996).

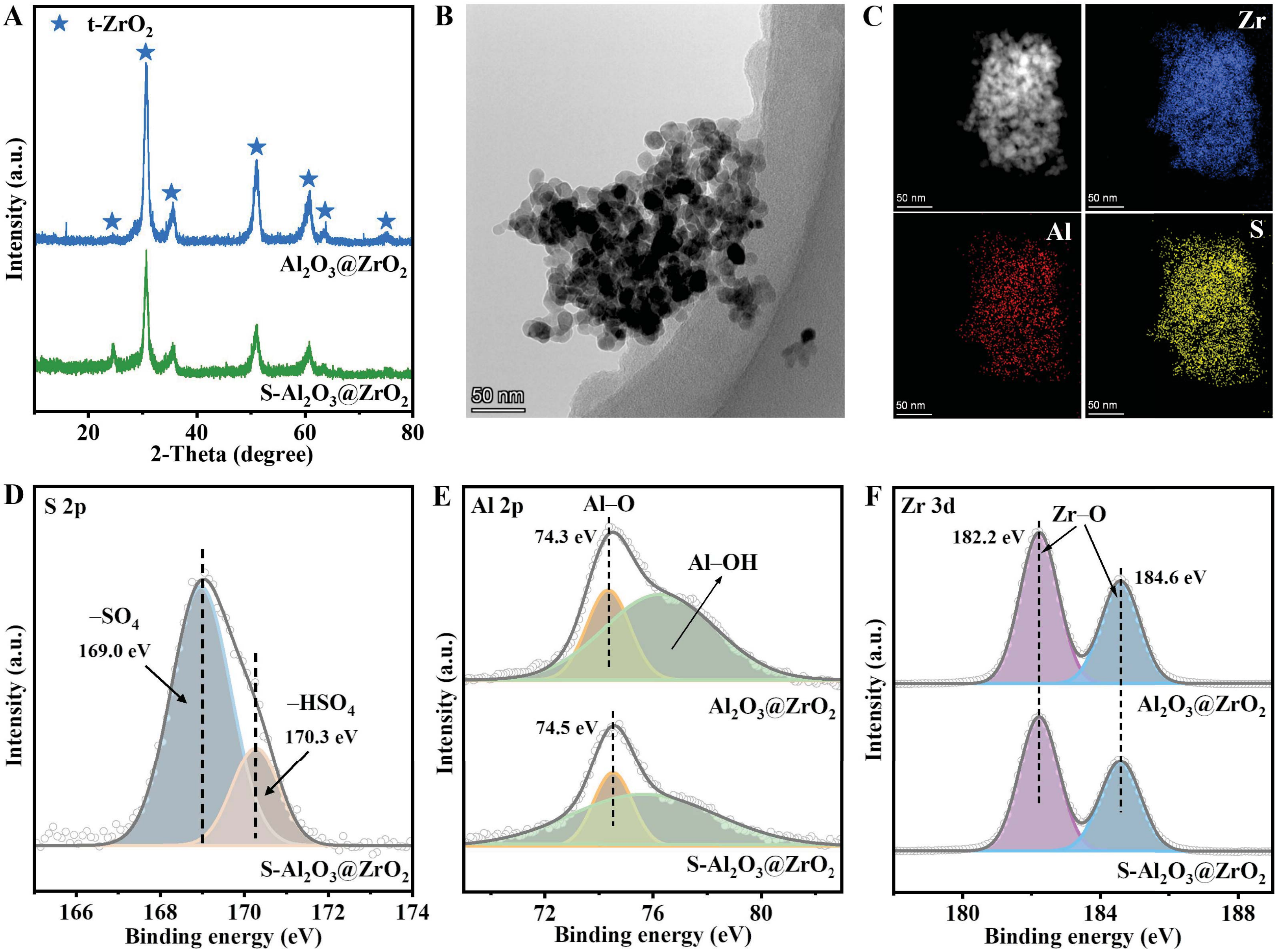
A
t-ZrO$_2$
Intensity (a.u.)
Al$_2$O$_3$@ZrO$_2$
S-Al$_2$O$_3$@ZrO$_2$
20
40
60
80
2-Theta (degree)
B
50 nm
C
Zr
Al
S
50 nm
D
S 2p
–SO$_4$
169.0 eV
–HSO$_4$
170.3 eV
Intensity (a.u.)
S-Al$_2$O$_3$@ZrO$_2$
166
168
170
172
174
Binding energy (eV)
E
Al 2p
Al–O
74.3 eV
Al–OH
Al$_2$O$_3$@ZrO$_2$
74.5 eV
S-Al$_2$O$_3$@ZrO$_2$
Intensity (a.u.)
72
76
80
Binding energy (eV)
F
Zr 3d
Zr–O
182.2 eV
184.6 eV
Al$_2$O$_3$@ZrO$_2$
S-Al$_2$O$_3$@ZrO$_2$
Intensity (a.u.)
180
184
188
Binding energy (eV)

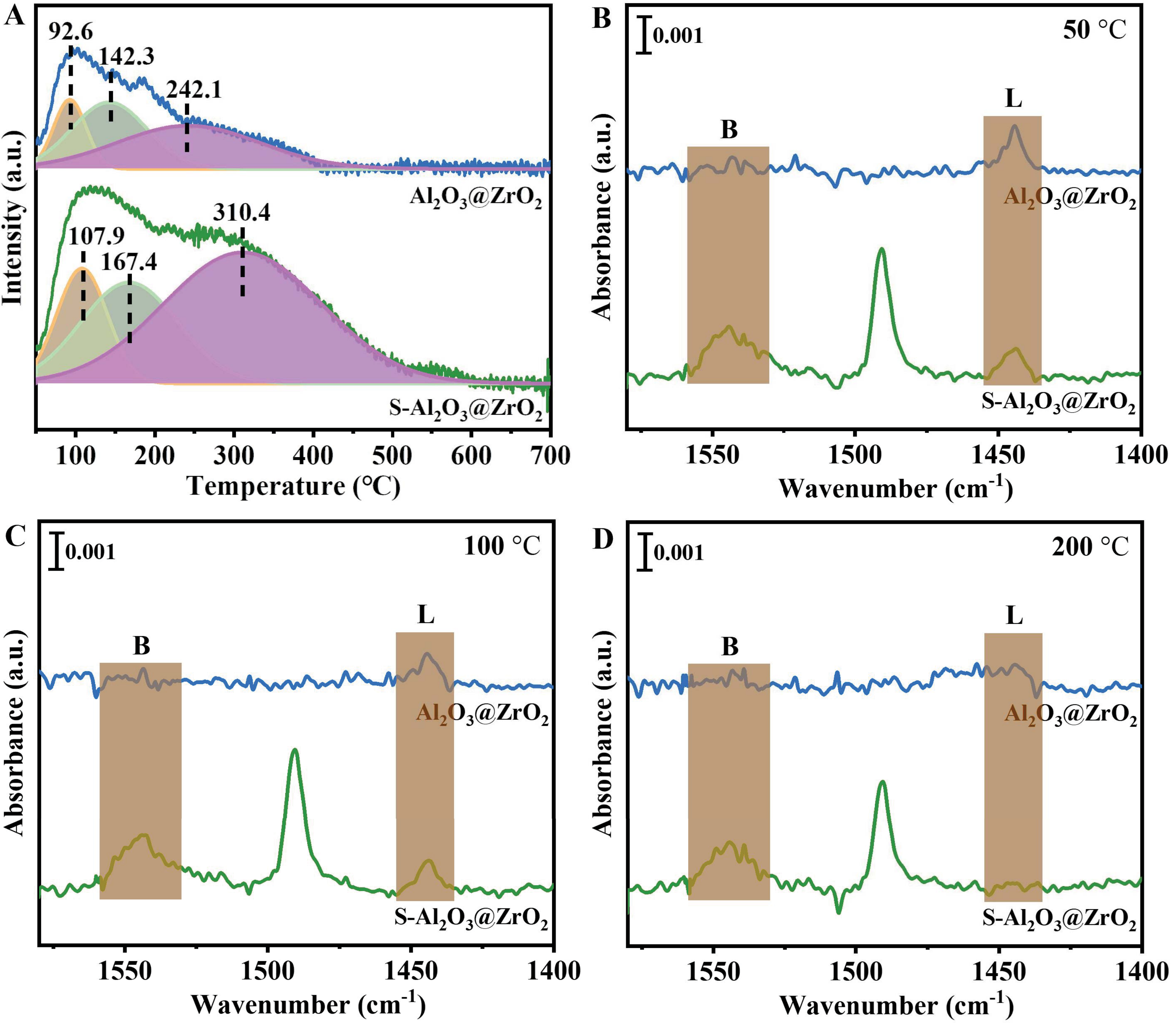
A
92.6
142.3
242.1
$Al_2O_3@ZrO_2$
310.4
107.9
167.4
$S-Al_2O_3@ZrO_2$
Intensity (a.u.)
100
200
300
400
500
600
700
Temperature (°C)
B
0.001
50 °C
B
L
$Al_2O_3@ZrO_2$
$S-Al_2O_3@ZrO_2$
Absorbance (a.u.)
1550
1500
1450
1400
Wavenumber (cm^{-1})
C
0.001
100 °C
B
L
$Al_2O_3@ZrO_2$
$S-Al_2O_3@ZrO_2$
Absorbance (a.u.)
1550
1500
1450
1400
Wavenumber (cm^{-1})
D
0.001
200 °C
B
L
$Al_2O_3@ZrO_2$
$S-Al_2O_3@ZrO_2$
Absorbance (a.u.)
1550
1500
1450
1400
Wavenumber (cm^{-1})

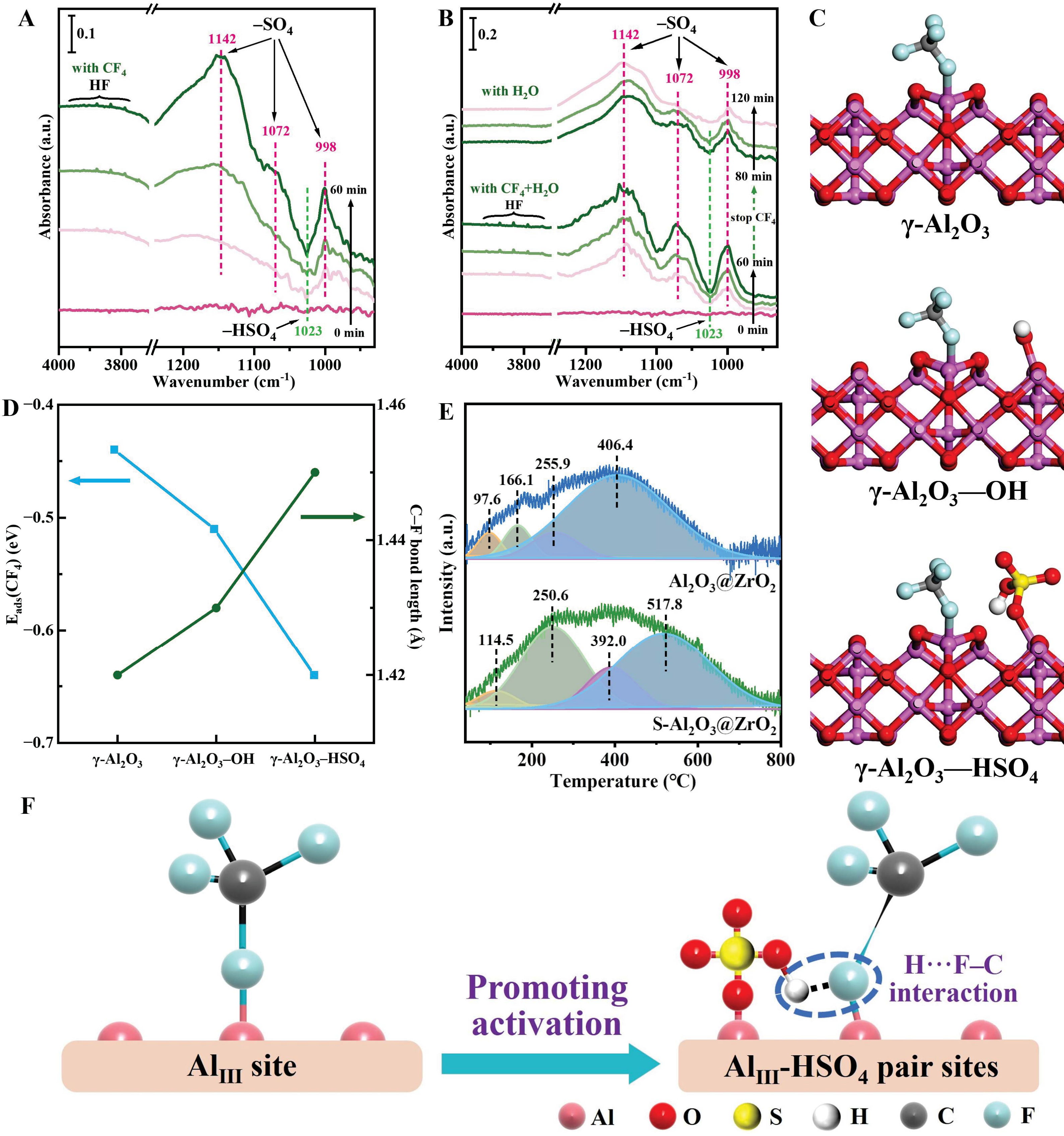
A
0.1
with CF_4
HF
$-SO_4$
1142
1072
998
60 min
$-HSO_4$
1023
0 min
Absorbance (a.u.)
4000
3800
1200
1100
1000
Wavenumber (cm^{-1})
B
0.2
$-SO_4$
1142
1072
998
with H_2O
120 min
80 min
with CF_4+H_2O
HF
stop CF_4
60 min
$-HSO_4$
1023
0 min
Absorbance (a.u.)
4000
3800
1200
1100
1000
Wavenumber (cm^{-1})
C
γ-Al_2O_3
γ-Al_2O_3—OH
γ-Al_2O_3—HSO_4
D
−0.4
−0.5
−0.6
−0.7
$E_{ads}(CF_4)$ (eV)
1.46
1.44
1.42
C–F bond length (Å)
γ-Al_2O_3
γ-Al_2O_3–OH
γ-Al_2O_3–HSO_4
E
97.6
166.1
255.9
406.4
Al_2O_3@ZrO_2
114.5
250.6
392.0
517.8
S-Al_2O_3@ZrO_2
Intensity (a.u.)
200
400
600
800
Temperature (°C)
F
Al_{III} site
Promoting activation
H···F–C interaction
Al_{III}-HSO_4 pair sites
Al
O
S
H
C
F

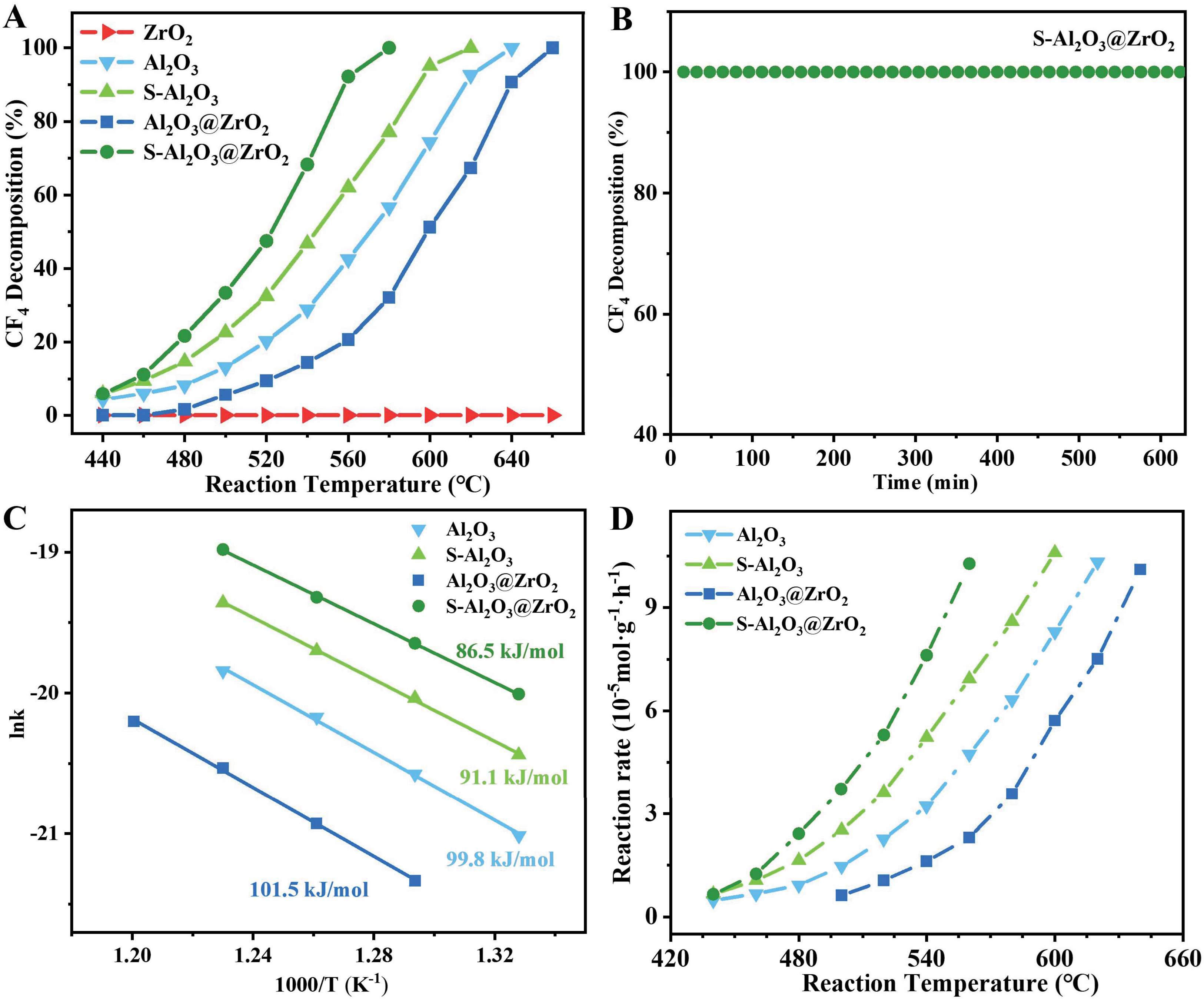
A
ZrO$_2$
Al$_2$O$_3$
S-Al$_2$O$_3$
Al$_2$O$_3$@ZrO$_2$
S-Al$_2$O$_3$@ZrO$_2$
CF$_4$ Decomposition (%)
0
20
40
60
80
100
440
480
520
560
600
640
Reaction Temperature (°C)
B
S-Al$_2$O$_3$@ZrO$_2$
CF$_4$ Decomposition (%)
40
60
80
100
0
100
200
300
400
500
600
Time (min)
C
Al$_2$O$_3$
S-Al$_2$O$_3$
Al$_2$O$_3$@ZrO$_2$
S-Al$_2$O$_3$@ZrO$_2$
86.5 kJ/mol
91.1 kJ/mol
99.8 kJ/mol
101.5 kJ/mol
lnk
-19
-20
-21
1.20
1.24
1.28
1.32
1000/T (K^{-1})
D
Al$_2$O$_3$
S-Al$_2$O$_3$
Al$_2$O$_3$@ZrO$_2$
S-Al$_2$O$_3$@ZrO$_2$
Reaction rate (10^{-5}mol·g^{-1}·h^{-1})
0
3
6
9
420
480
540
600
660
Reaction Temperature (°C)

Supporting Information for

Promoting C–F bond activation via proton donor for CF_4 decomposition

Yingkang Chen[a], Wenqiang Qu[b], Tao Luo[a], Hang Zhang[a], Junwei Fu[a], Hongmei Li[a], Changxu Liu[c], Dengsong Zhang[b], and Min Liu[a,*]
[a] Hunan Joint International Research Center for Carbon Dioxide Resource Utilization, School of Physics, and School of Metallurgy and Environment, Central South University, Changsha 410083, Hunan, P. R. China
[b] International Joint Laboratory of Catalytic Chemistry, Department of Chemistry, College of Sciences, Shanghai University, Shanghai 200444, P. R. China
[c] Centre for Metamaterial Research & Innovation, Department of Engineering, University of Exeter, Exeter EX4 4QF, United Kingdom

*Min Liu
Email: minliu@csu.edu.cn

This PDF file includes:

Figures S1 to S26
Tables S1 to S9
SI References

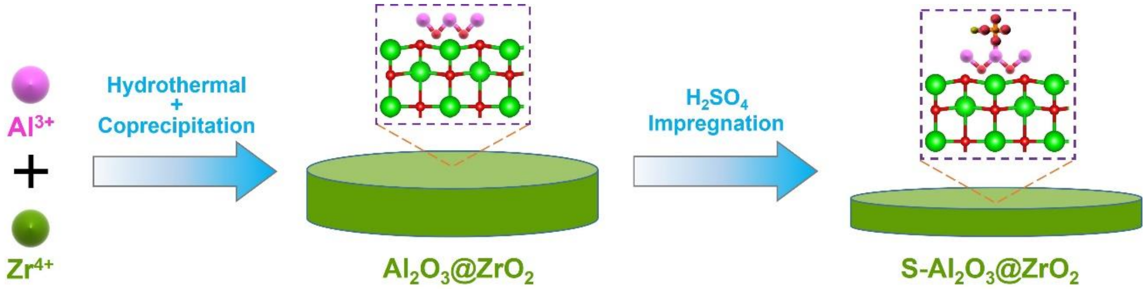

Fig. S1. Schematic illustration of the synthesis process of S-Al_2O_3@ZrO_2 catalyst.

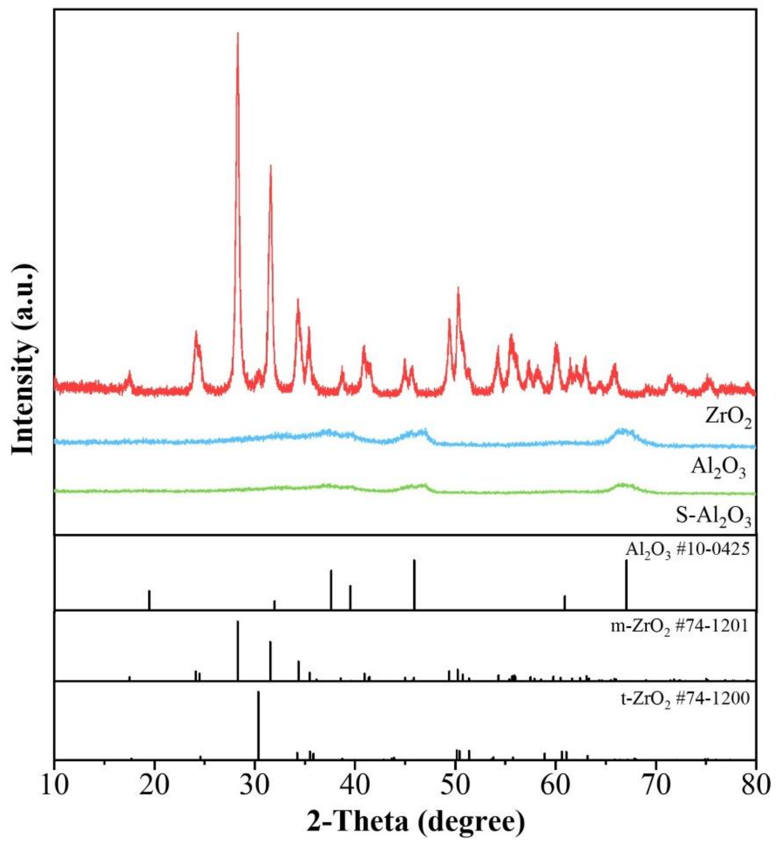

Fig. S2. XRD patterns of ZrO_2, Al_2O_3 and S-Al_2O_3 catalysts.

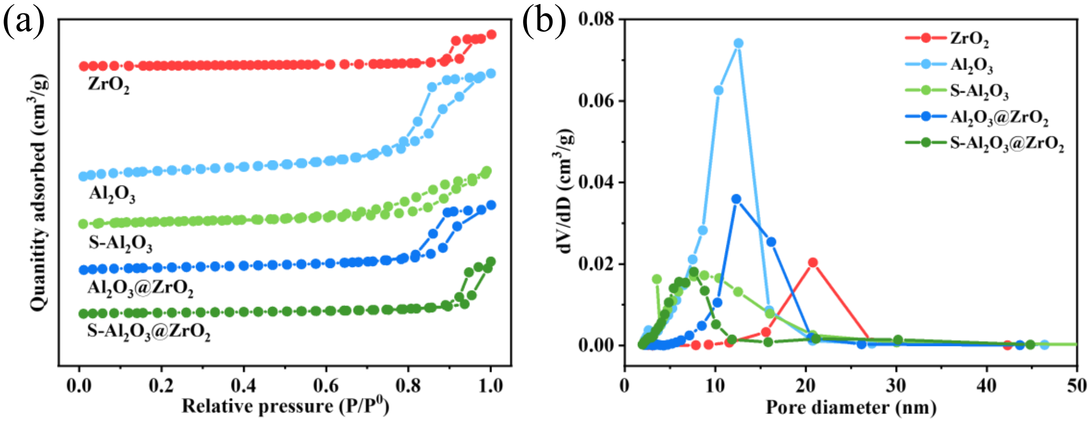

Fig. S3. (a) N_2 adsorption−desorption curve and (b) pore diameter distribution of ZrO_2, Al_2O_3, S-Al_2O_3, Al_2O_3@ZrO_2 and S-Al_2O_3@ZrO_2 catalysts.

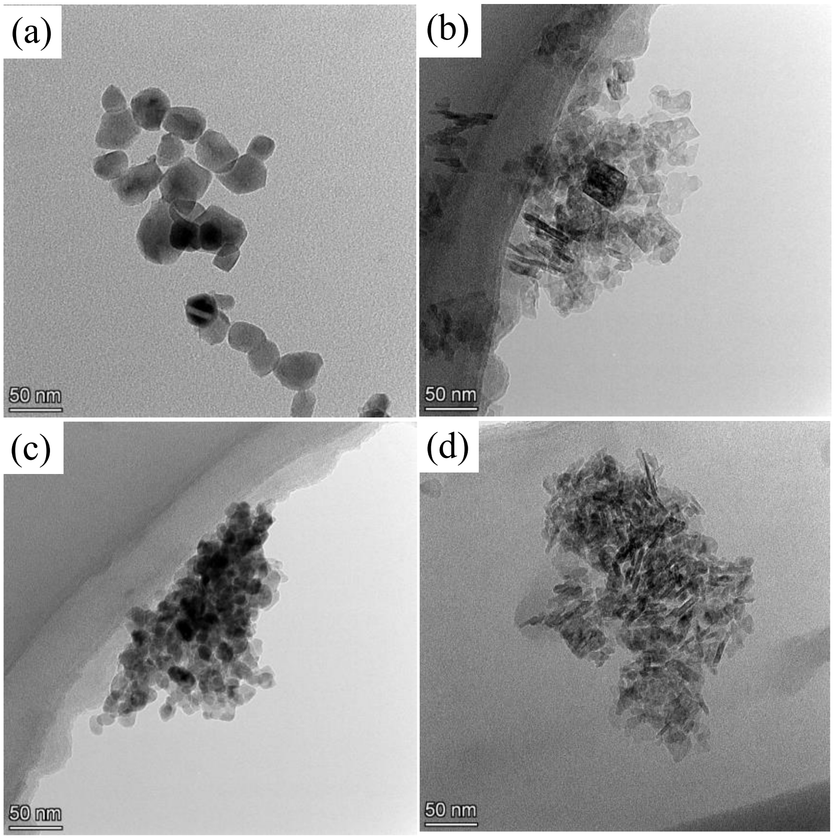

Fig. S4. TEM images of (a) ZrO_2, (b) Al_2O_3, (c) Al_2O_3@ZrO_2 and (d) S-Al_2O_3 catalysts.

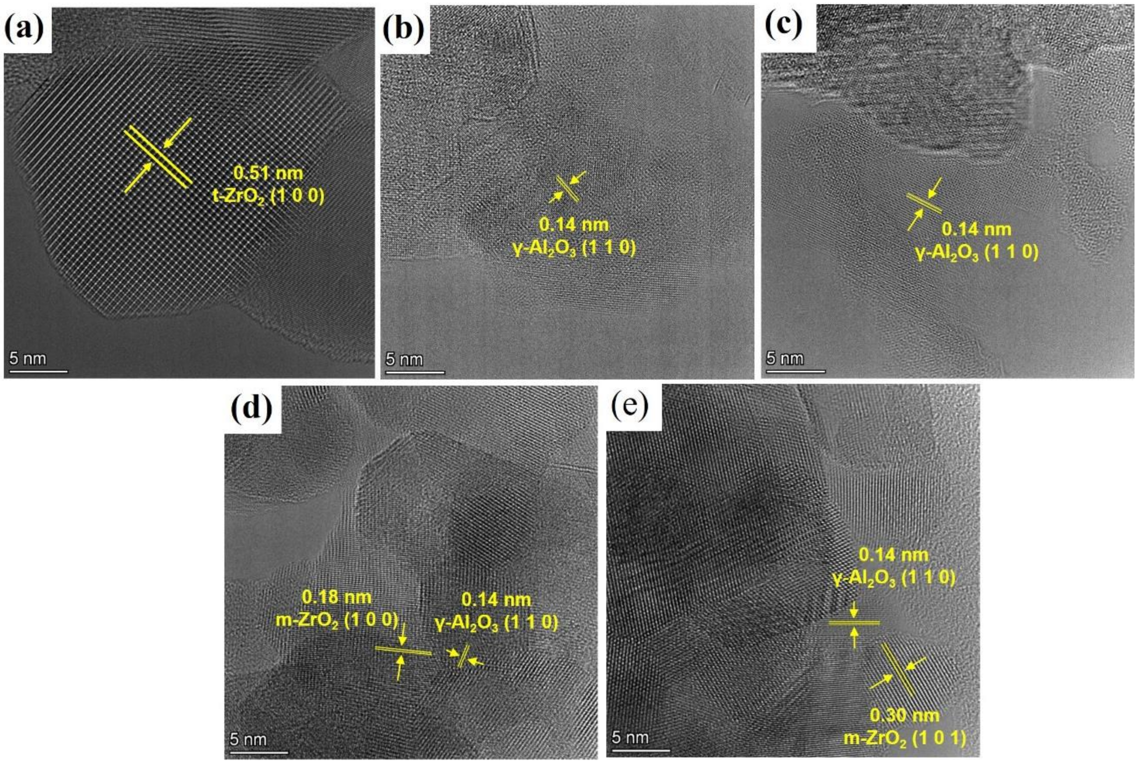

Fig. S5. HRTEM images of (a) ZrO_2, (b) Al_2O_3, (c) S-Al_2O_3, (d) Al_2O_3@ZrO_2 and (e) S-Al_2O_3@ZrO_2 catalysts.

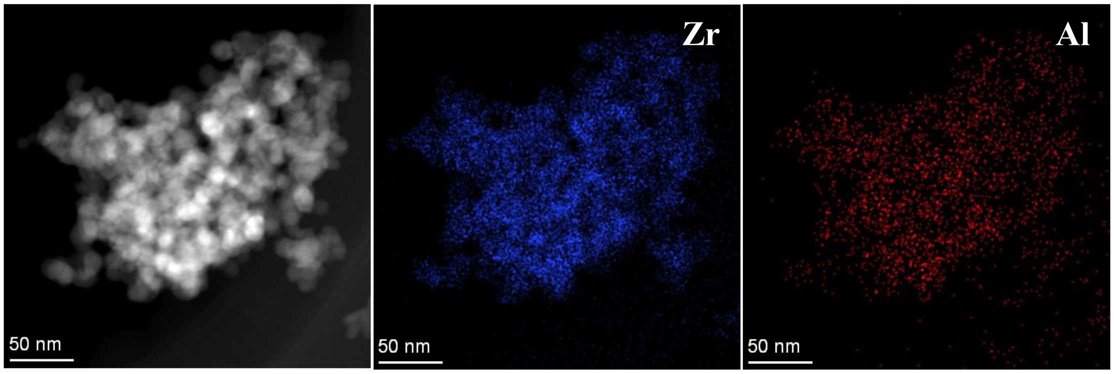

Fig. S6. EDS mapping images of Al_2O_3@ZrO_2 catalyst.

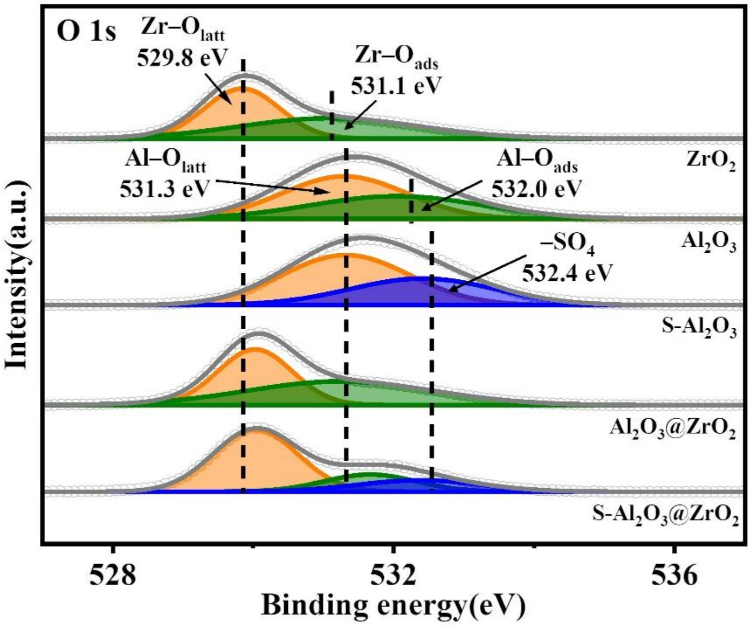

Fig. S7. XPS spectra of O 1s for ZrO$_2$, Al$_2$O$_3$, S-Al$_2$O$_3$, Al$_2$O$_3$@ZrO$_2$ and S-Al$_2$O$_3$@ZrO$_2$ catalysts.

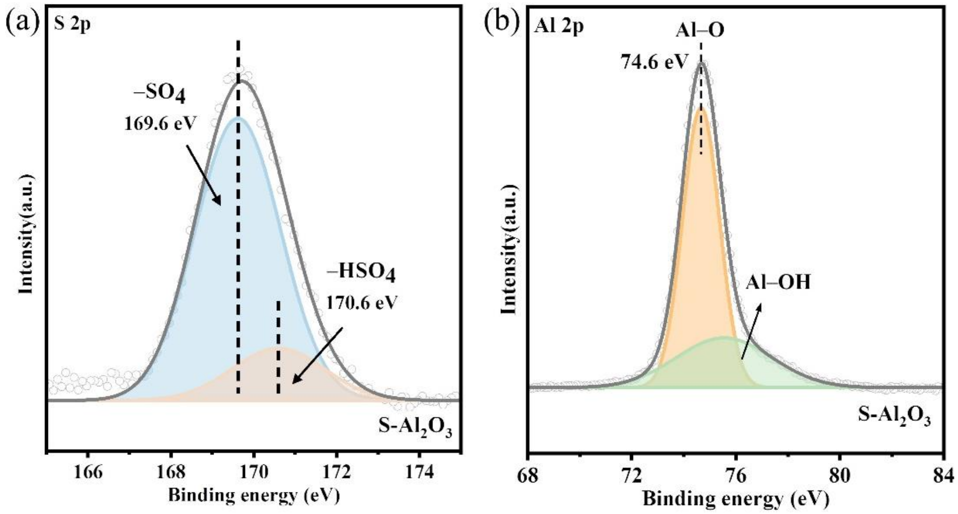

Fig. S8. XPS spectra of (a) Al 2p and (b) S 2p for S-Al_2O_3 catalyst.

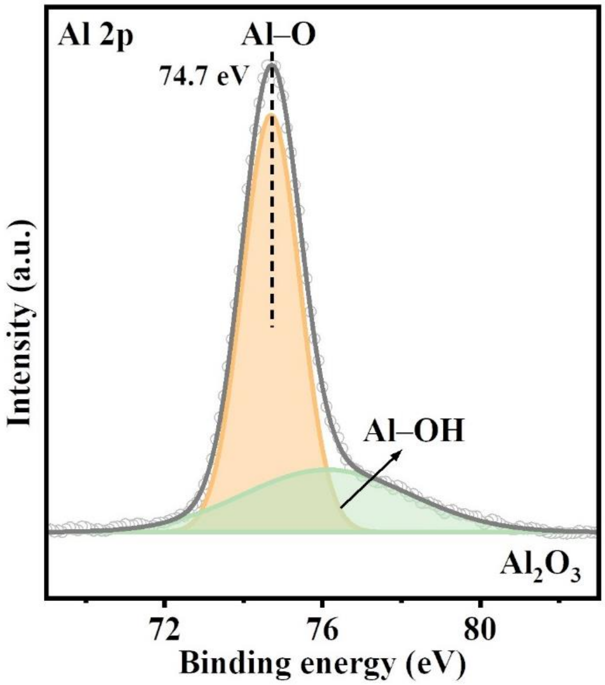

Fig. S9. XPS spectra of Al 2p for Al_2O_3.

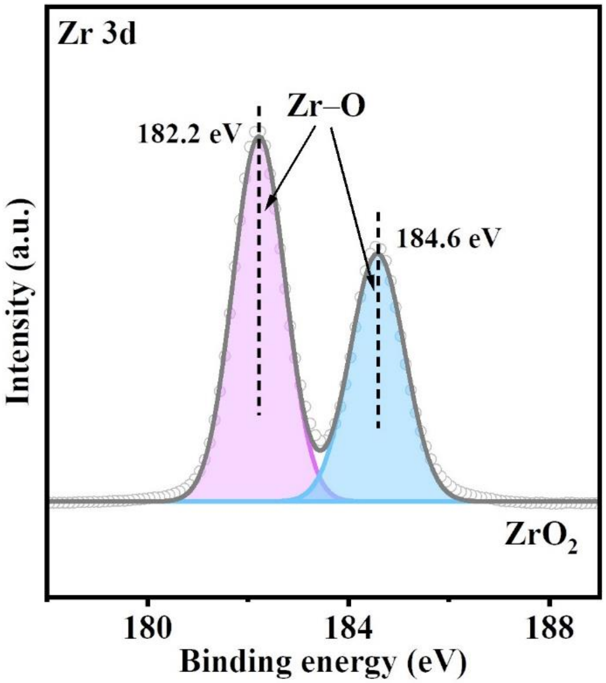

Fig. S10. XPS spectra of Zr 3d for ZrO$_2$.

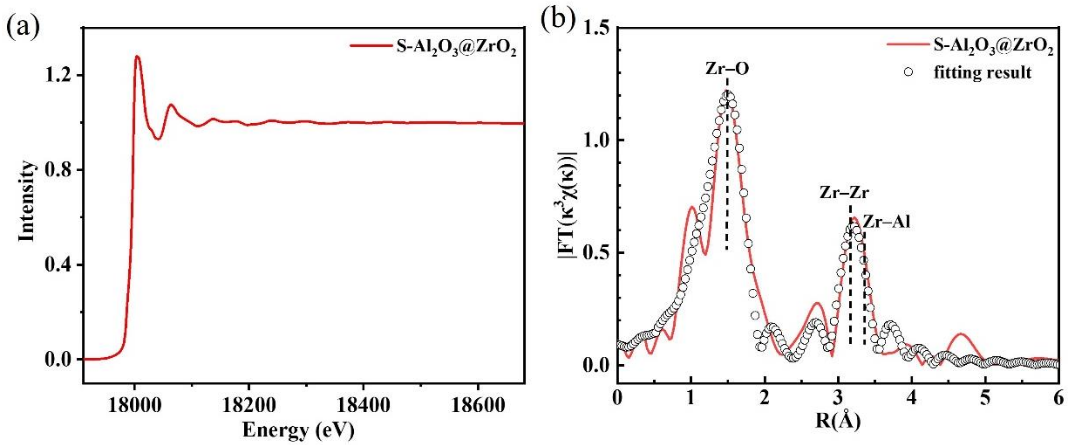

Fig. S11. The Zr k-edge (a) XAS spectrum and (b) XAFS fitting result of S-Al_2O_3@ZrO_2 catalyst.

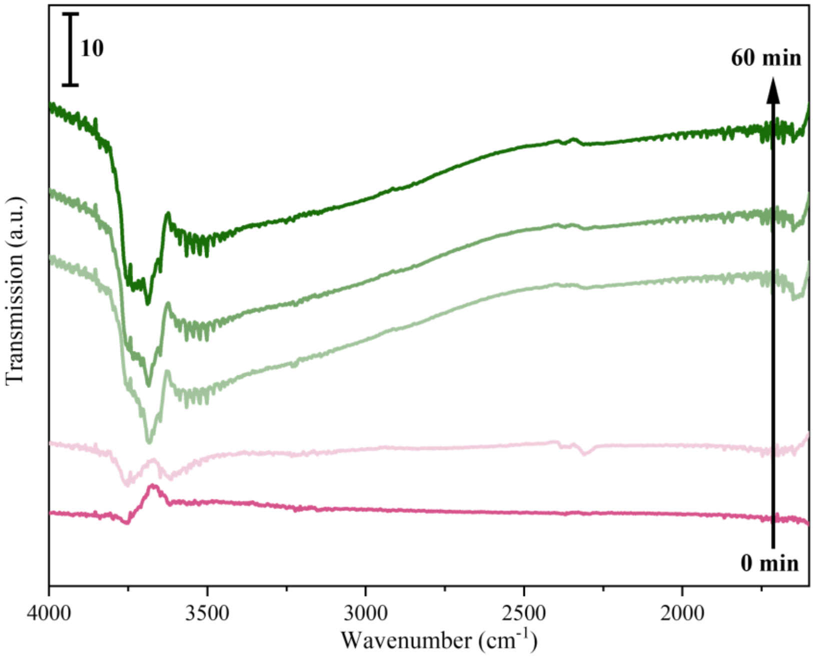

Fig. S12. *In situ* IR spectra of $Al_2O_3@ZrO_2$ catalyst with H_2O at 580 °C.

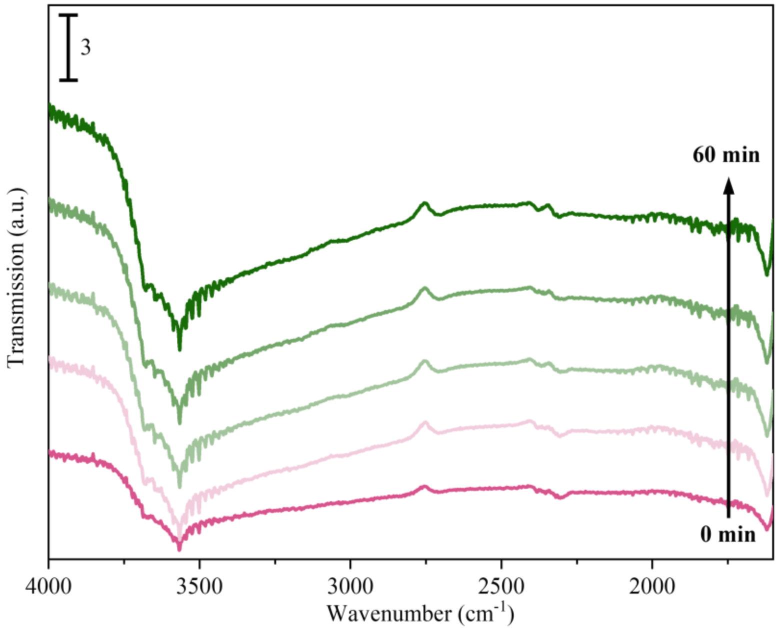

Fig. S13. *In situ* IR spectra of S-Al_2O_3@ZrO_2 catalyst with H_2O at 580 °C.

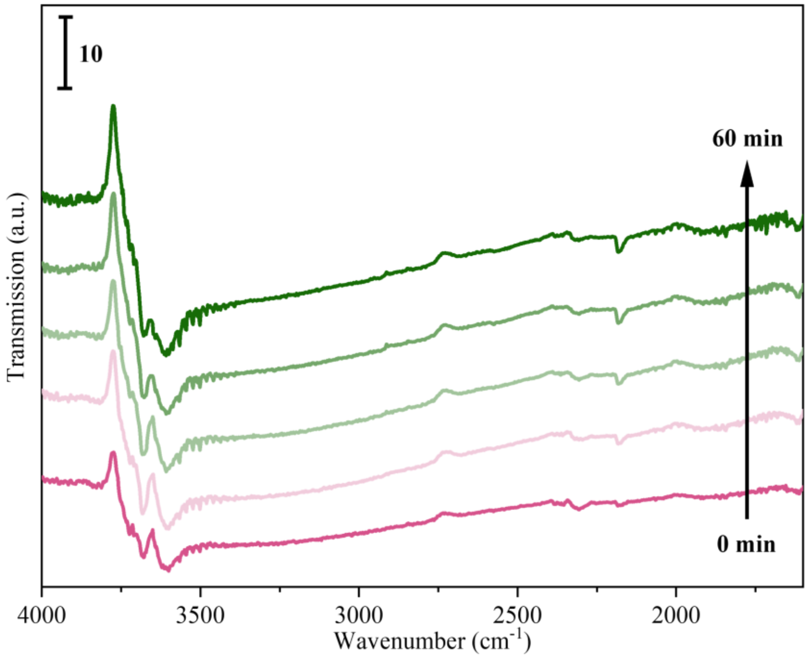

Fig. S14. *In situ* IR spectra of Al_2O_3@ZrO_2 catalyst with CF_4 and H_2O at 580 °C.

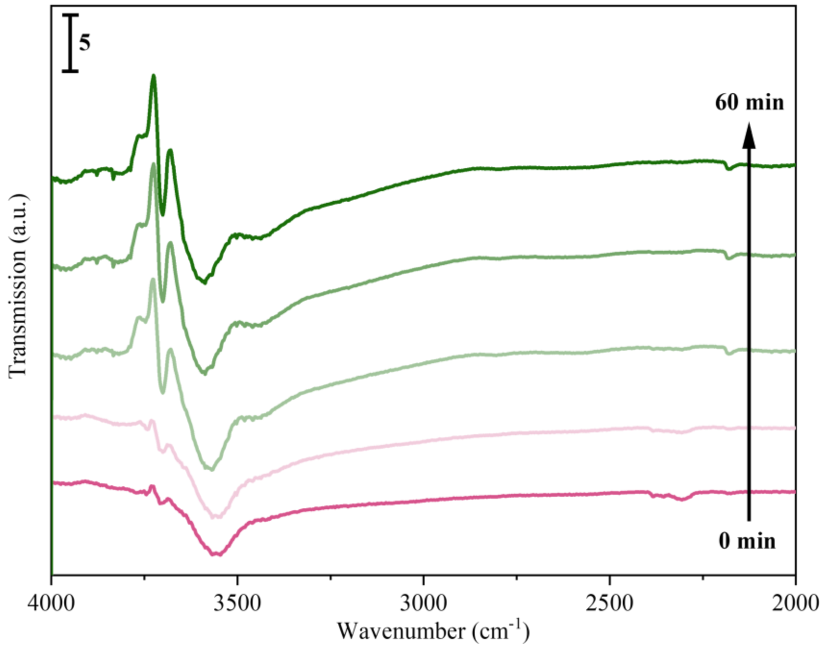

Fig. S15. *In situ* IR spectra of Al_2O_3 catalyst with CF_4 and H_2O at 580 °C.

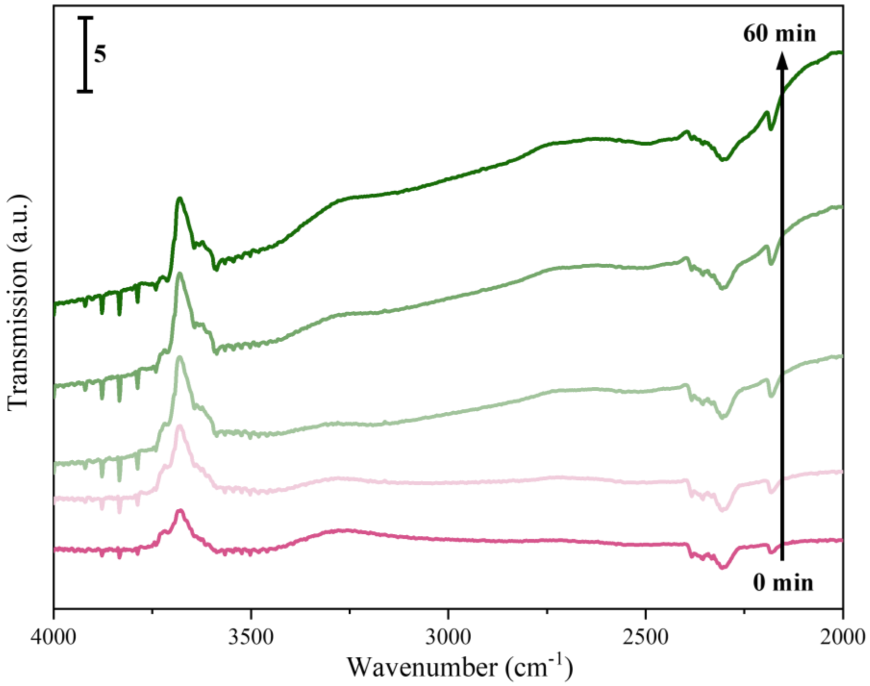

Fig. S16. *In situ* IR spectra of S-Al_2O_3 catalyst with CF_4 and H_2O at 580 °C.

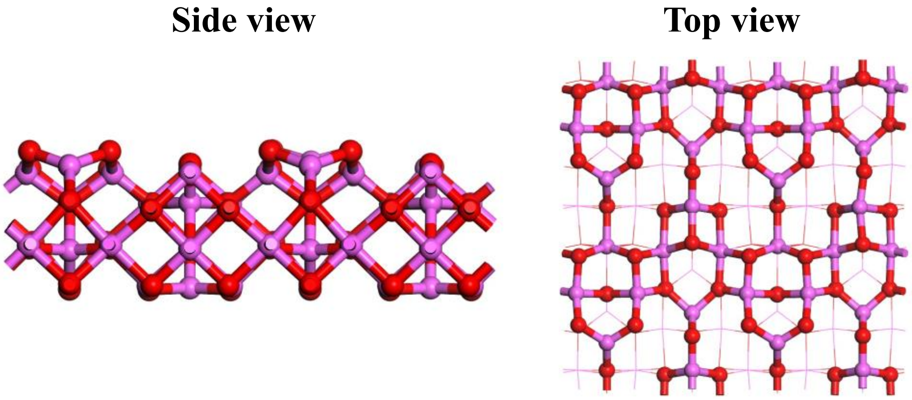

Fig. S17. The side view and top view of calculation model of γ-Al_2O_3 (110) face.

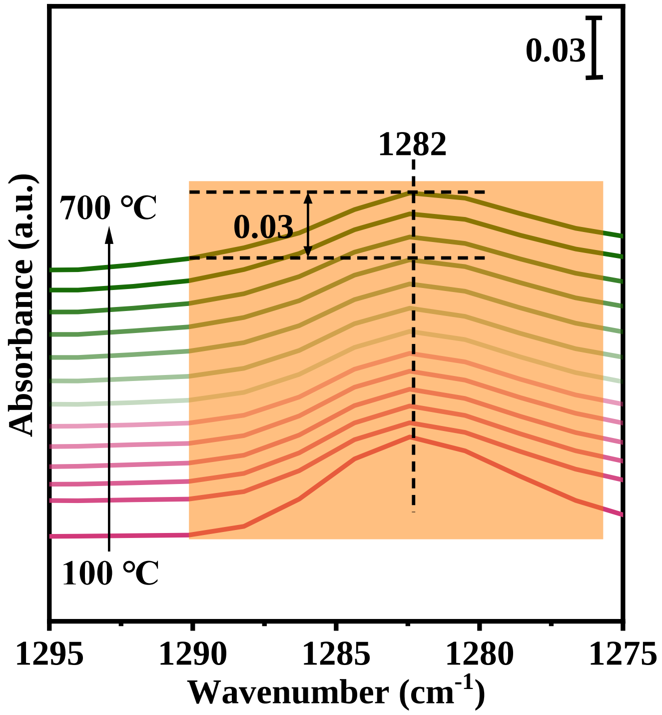

Fig. S18. *In situ* IR spectra of the desorption process of pre-adsorbed CF_4 on $Al_2O_3@ZrO_2$ from 100 to 700 °C.

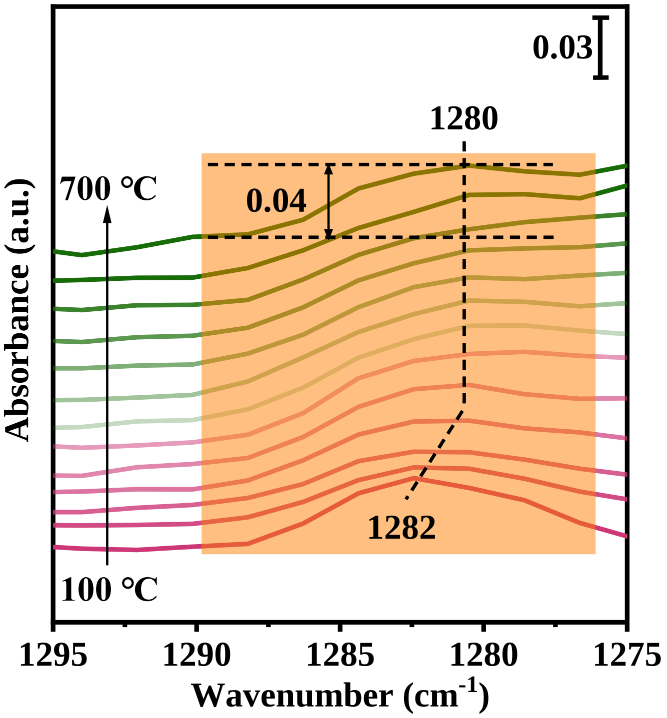

Fig. S19. *In situ* IR spectra of the desorption process of pre-adsorbed CF_4 on S-Al_2O_3@ZrO_2 from 100 to 700 °C.

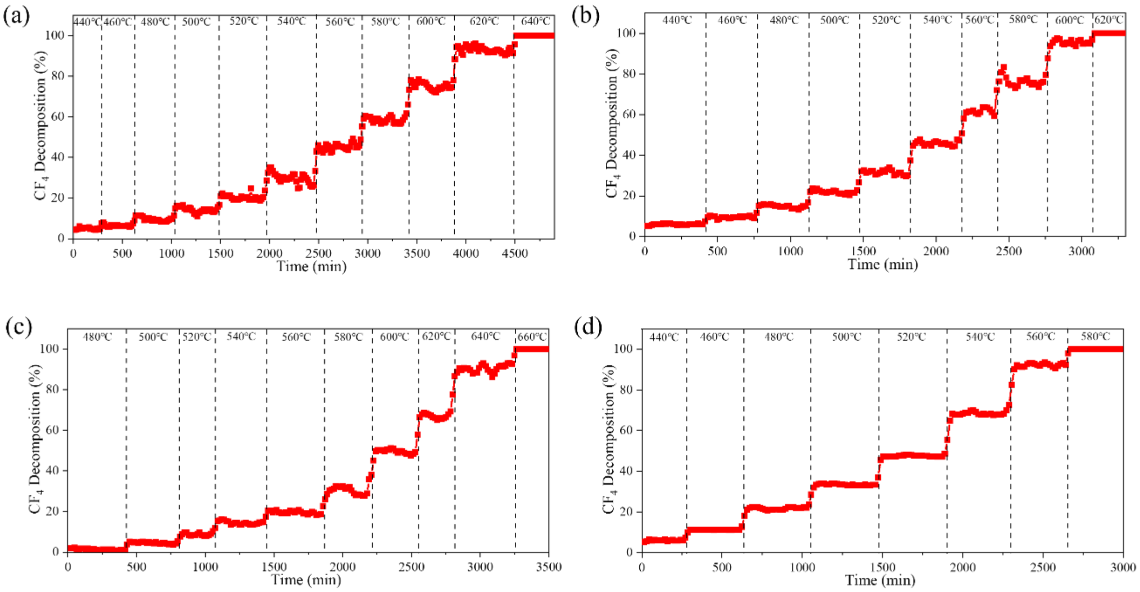

Fig. S20. The catalytic performance of (a) Al_2O_3, (b) S-Al_2O_3, (c) Al_2O_3@ZrO_2 and (d) S-Al_2O_3@ZrO_2 catalysts as a function of temperature. Reaction condition: 2500 ppm of CF_4 and 10% of H_2O balanced with Ar, total flow rate of 33.3 mL min^{-1}, and weight hourly space velocity (WHSV) of 1000 mL g^{-1} h^{-1}.

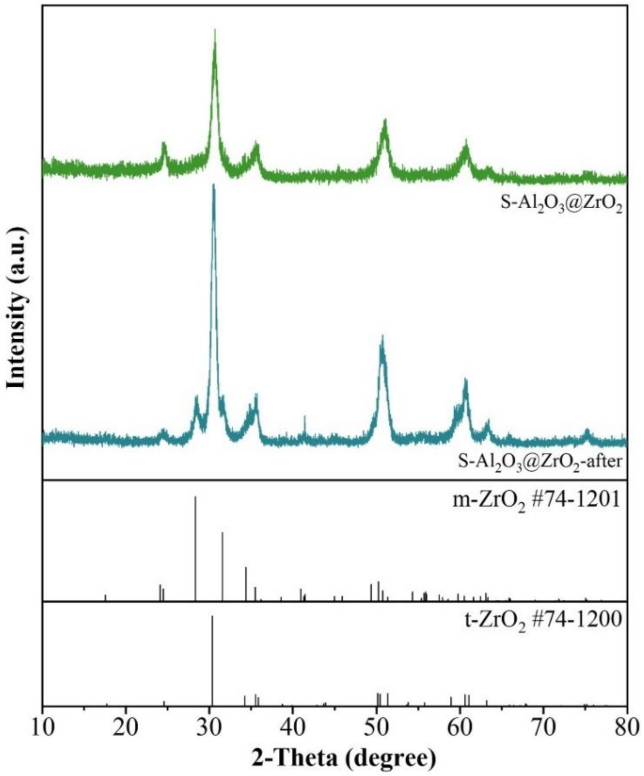

Fig. S21. XRD patterns of S-Al$_2$O$_3$@ZrO$_2$ catalyst before and after CF$_4$ decomposition.

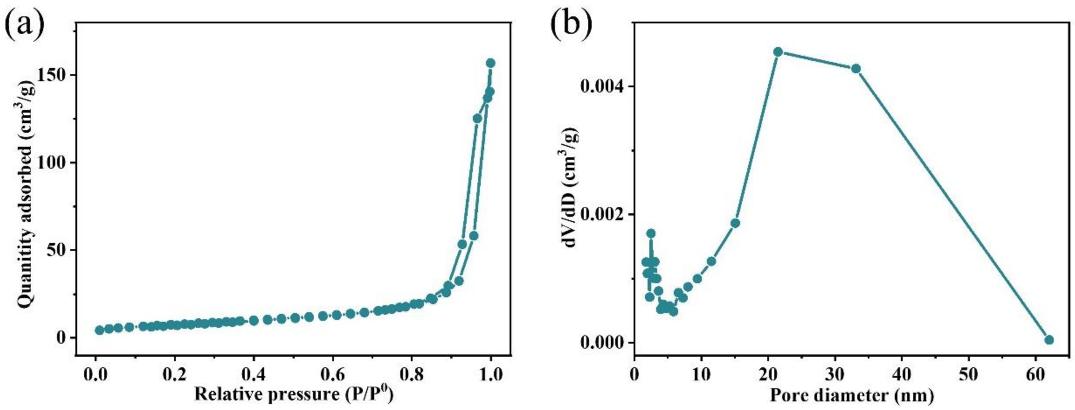

Fig. S22. (a) N_2 adsorption−desorption curve and (b) pore diameter distribution of S-Al_2O_3@ZrO_2-after catalyst.

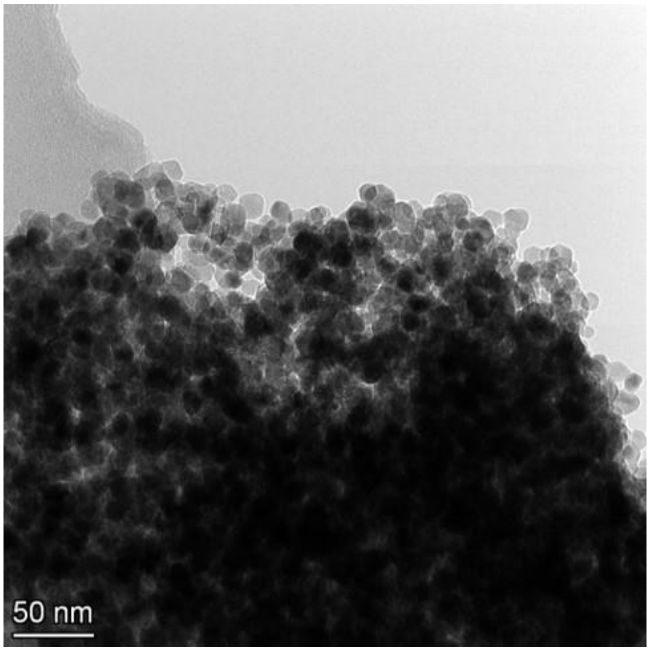

Fig. S23. TEM image of S-Al_2O_3@ZrO_2-after catalyst.

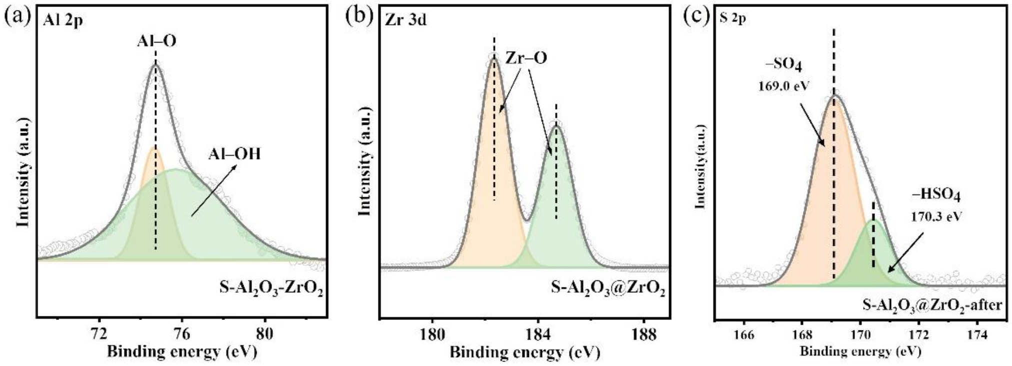

Fig. S24. XPS spectra of (a) Al 2p, (b) Zr 3d and (c) S 2p for S-Al$_2$O$_3$@ZrO$_2$-after catalyst.

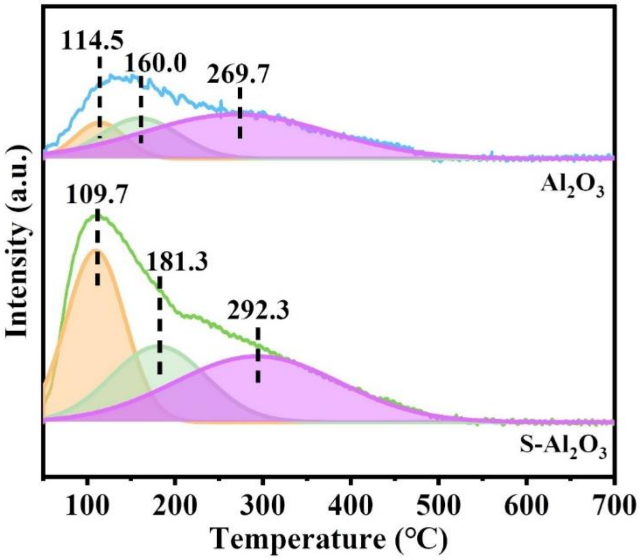

Fig. S25. NH$_3$-TPD profiles of the Al$_2$O$_3$ and S-Al$_2$O$_3$ catalysts.

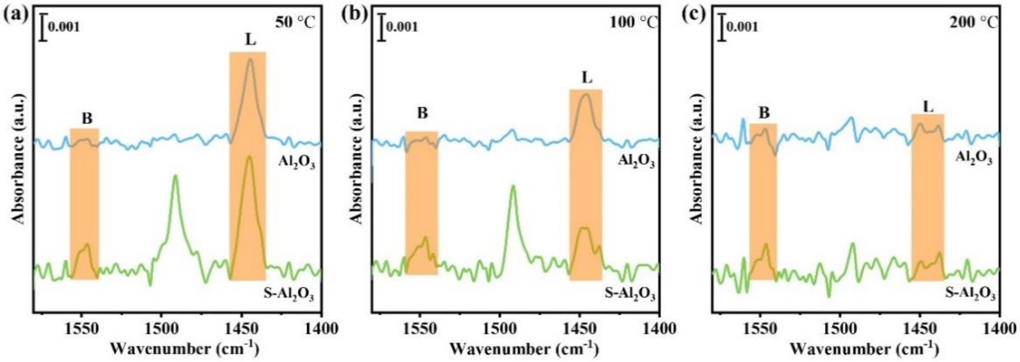

Fig. S26. Py-IR spectra of the Al_2O_3 and S-Al_2O_3 at (a) 50 °C, (b) 100 °C and (c) 200 °C desorption temperature.

Table S1. BET results of ZrO_2, Al_2O_3, S-Al_2O_3, Al_2O_3@ZrO_2 and S-Al_2O_3@ZrO_2 catalysts.

Sample	SA (m^2 g^{-1})	PV (cm^3 g^{-1})	APR (nm)
ZrO_2	18.6	0.13	24.1
Al_2O_3	136.7	0.47	11.9
S-Al_2O_3	40.5	0.09	8.5
Al_2O_3@ZrO_2	61.3	0.21	12.1
S-Al_2O_3@ZrO_2	49.8	0.13	9.3

Table S2. XPS results of ZrO_2, Al_2O_3, S-Al_2O_3, Al_2O_3@ZrO_2 and S-Al_2O_3@ZrO_2 catalysts.

Sample	Al 2p (%)	Zr 3d (%)	O 1s (%)	S 2p (%)		$–HSO_4$/$–SO_4$ ratio
				$–SO_4$	$–HSO_4$	
ZrO_2	-	26.02	73.98	-	-	-
Al_2O_3	40.99	-	59.01	-	-	-
S-Al_2O_3	38.48	-	57.80	3.10	0.62	0.20
Al_2O_3@ZrO_2	19.24	20.08	60.68	-	-	-
S-Al_2O_3@ZrO_2	14.25	19.25	63.17	2.56	0.77	0.30

Table S3. Fitting Results of Zr K-edge EXAFS Data.

Sample	R_{Zr-O}	N_{Zr-O}	R_{Zr-Zr}	N_{Zr-Zr}	R_{Zr-Al}	N_{Zr-Al}
S-Al_2O_3@ZrO_2	2.12	4.83	3.33	6.75	3.74	2.08

Table S4. Acidity data obtained from NH_3-TPD and py-IR measurements.

Sample	Acidity (μmol g^{-1})			L/B ratio [a]
	Total	weak	medium	
Al_2O_3	18.76	7.05	11.71	-
S-Al_2O_3	40.03	24.53	15.50	1.34
Al_2O_3@ZrO_2	7.86	4.23	3.63	-
S-Al_2O_3@ZrO_2	21.28	9.17	12.11	0.28

a Determined by the normalized peak areas at 1444 cm^{-1} and 1544 cm^{-1} of the py-IR spectra after desorption at 100 °C.

Table S5. Catalytic activity for CF_4 hydrolysis over previous studies.

Catalyst	Temperature (°C)	Stable CF_4 decomposition	Ref.
Ce10%-$AlPO_4$	700	100%	(1)
Ga-Al	680	97%	(2)
$AlPO_4$-Al_2O_3	750	100%	(3)
γ-Al_2O_3	750	100%	(3)
Ga20-Al_2O_3	630	84%	(4)
Ga20S10-Al_2O_3	630	98%	(4)
ZnO/γ-Al_2O_3	650	99.4%	(5)
5%Cu-MCM-41	850	70%	(6)
5%Fe-MCM-41	800	81%	(7)
16%Zr/Al_2O_3	650	85%	(8)
S-Al_2O_3@ZrO_2	580	100%	This work

Table S6. BET and ICP-OES results of S-Al_2O_3@ZrO_2 catalyst after CF_4 decomposition.

Samples	SA (m^2 g^{-1})	PV (cm^3 g^{-1})	APR (nm)	Al content (wt.%)	S content (wt.%)
S-Al_2O_3@ZrO_2-after	27.3	0.09	30.4	2.903	0.18

Table S7. XPS results of S-Al_2O_3@ZrO_2-after catalysts.

Sample	Al 2p (%)	Zr 3d (%)	O 1s (%)	S 2p (%)		–HSO_4/ –SO_4 ratio
				–SO_4	–HSO_4	
S-Al_2O_3@ZrO_2-after	14.25	19.25	63.17	2.56	0.77	0.30

Table S8. ICP-OES results of Al_2O_3, S-Al_2O_3, Al_2O_3@ZrO_2 and S-Al_2O_3@ZrO_2 catalysts.

Sample	Al content (wt.%)	S content (wt.%)
Al_2O_3	56.75	-
S-Al_2O_3	55.53	4.56
Al_2O_3@ZrO_2	2.99	-
S-Al_2O_3@ZrO_2	2.87	4.36

Table S9. Details of the TOF calculation for catalytic CF_4 decomposition.

Sample	surface Al_{III} ^{a} (μmol)	CF_4 decomposition ^{b} (%)	TOF ^{c} (10^{-3} s^{-1})
Al_2O_3	23.42	13.2	0.35
S-Al_2O_3	17.75	22.6	0.79
Al_2O_3@ZrO_2	7.26	5.6	0.47
S-Al_2O_3@ZrO_2	5.29	33.4	3.91

a Determined by the NH_3-TPD and py-IR result.

Calculation equation: $[\text{surface Al}_{\text{III}}]=[\text{medium acidity } (\mu\text{mol g}^{-1})] \times [\text{L/L+B}]$

b CF_4 decomposition at 500 °C (2.0 g catalyst, 2500 ppm of CF_4 and 10% of H_2O balanced with Ar, 33.3 mL min^{-1}).

c Turnover frequency of the CF_4 decomposition at 500 °C.

Calculation equation: $\text{TOF}=\dfrac{[\text{CF}_4 \text{ flow rate } (\mu\text{mol s}^{-1})] \times [\text{CF}_4 \text{ decomposition}]}{[\text{surface Al}_{\text{III}}]}$

SI References

1. Y. Takita, C. Morita, M. Ninomiya, Catalytic decomposition of CF_4 over $AlPO_4$-based catalysts. *Chem. Lett.* **28**, 417-418 (1999).
2. Z M El-Bahy, R Ohnishi, M Ichikawa, Hydrolysis of CF_4 over alumina-based binary metal oxide catalysts. *Applied Catalysis B: Environmental* **40**, 81-91 (2003).
3. J Y Jeon, X F Xu, M H Choi, H Y Kim, Y K Park, Hydrolytic decomposition of PFCs over $AlPO_4$–Al_2O_3 catalyst. *Chemical Communications* 1244-5 (2003).
4. Z. M. El-Bahy, R. Ohnishi, M. Ichikawa, Hydrolytic decomposition of CF_4 over alumina-based binary metal oxide catalysts: high catalytic activity of gallia-alumina catalyst. *Catal. Today* **90**, 283-290 (2004).
5. T. Sasaki, S. Kanno, Role of acid sites on γ-Al_2O_3 based catalyst for CF_4 hydrolysis. *Kag. Kog. Ronbunshu* **37**, 175-180 (2011).
6. J. Han, A. Shiue, Y. Shiue, D. Huang, C. C. Chang, Catalytic decomposition of CF_4 over copper promoted mesoporous catalysts. *Sustain. Environ. Res.* **23**, 307-314 (2013).
7. C. Chen, A;. Shiue, D. Huang, C. C. Chang, Catalytic decomposition of CF_4 over iron promoted mesoporous catalysts. *J. Nanosci. Nanotechno.* **14**, 3202-3208 (2014).
8. X. Zheng, K;. Xiang, F. Shen, H. Liu, The Zr modified γ-Al_2O_3 catalysts for stable hydrolytic decomposition of CF_4 at low temperature. *Catalysts* **12**, 313 (2022).